DYNAMICS OF THE AUSTRALIAN SUMMER MONSOON

Wayne H. Schubert, Paul E. Ciesielski and Kenneth W. Harding

Colorado State University

DEPARTMENT OF ATMOSPHERIC SCIENCE

PAPER NO. 492

DYNAMICS OF THE AUSTRALIAN SUMMER MONSOON

Wayne H. Schubert
Paul E. Ciesielski
Kenneth W. Harding

Department of Atmospheric Science
Colorado State University
Fort Collins, Colorado 80523

6 March 1992

Atmospheric Science Paper 492

ABSTRACT

When a west-east line of deep convection forms over northern Australia, the potential vorticity field begins to change due to the latent heat release, with low level negative and upper level positive anomalies being induced. These potential vorticity patterns can be analytically derived by using a zonal balance model formulated in isentropic and potential latitude coordinates. The associated wind and mass fields can be found by solving an invertibility principle which is valid for these equatorial balanced flows. Since the convectively induced potential vorticity anomalies develop from an initial state which has potential vorticity increasing toward the north, reversed poleward gradients of potential vorticity are produced. The regions of potential vorticity gradient reversal are found on the poleward side of the ITCZ at low levels and on the equatorward side of the ITCZ at upper levels, just as in the observed fields during AMEX. For typical convective heating rates, significant potential vorticity gradient reversals occur quickly—on the order of a few days. This sets the stage for combined barotropic-baroclinic instability, the formation of tropical waves, and the breakdown of the ITCZ. We can understand the barotropic aspects of this breakdown through a normal mode stability analysis of the nondivergent barotropic model with either a hyperbolic tangent shear layer basic state zonal wind or an idealized three region profile in which there is a central (ITCZ) region of anomalous absolute vorticity, surrounded by regions of undisturbed absolute vorticity. The latter model can be solved analytically, which allows direct interpretation of the breakdown in terms of the phase locking and growth of the counterpropagating vorticity anomalies (essentially Rossby waves) located on the two interfaces separating the three regions. In this sense the ITCZ is self-destructive and should not be viewed as a strictly steady state feature of the tropical circulation. In addition, according to this scenario, the potential vorticity dynamics of the Australian region are not unique, but are characterized by an ITCZ formation-breakdown cycle similar to that occuring in other tropical regions such as the tropical east Pacific and western Africa.

1. Introduction

The purpose of the present paper is to show how the monsoon trough over northern Australia and its associated zonal circulation can be produced in just a few days by latent heat release in an elongated east-west line of ITCZ convection and then to examine how this zonal flow can become barotropically unstable. We shall model the basic potential vorticity (PV) dynamics of this process with a zonally symmetric, inviscid, balanced theory (section 3), and compare the model results with observed zonal wind and PV cross-sections (section 2) from the Australian Monsoon Experiment (AMEX). The zonal flows produced by this idealized Hadley cell model can then be analyzed for stability using linear and nonlinear stability theorems and normal mode methods (sections 4 and 5). This allows fluctuations in the monsoon trough to be interpreted in terms of dynamic instability associated with a reversal of the normal poleward gradient of potential vorticity on isentropic surfaces.

2. AMEX cross-sections of zonal wind and potential vorticity

General discussions of the climatology and interannual variability of the Australian summer monsoon can be found in Holland (1986), McBride (1987) and Hendon and Liebmann (1990). The particular sequence of weather events which occurred during the second phase of AMEX (10 January to 15 February 1987) has been described in detail by McBride and Holland (1989), Gunn et al. (1989), Hendon et al. (1989), Davidson et al. (1990), Webster and Houze (1991), and Mapes and Houze (1992). The average low-level flow during this period was characterized by a monsoon trough or shear line near 15 S, with westerlies to the north and easterlies to the south. After the monsoon westerlies had been established on 14 January, they were maintained throughout the AMEX period except for two break periods. Here we shall contrast the inactive monsoon period 25–29 January and the active period 30 January to 4 February. Meridional cross-sections of zonal wind for these two periods are presented in the bottom panels of Figs. 1 and 2. The winds shown here represent an average over the sector 110–135 E, which during the active period contained intense convection between 10 and 15 S. According to McBride et al. (1989) and Frank and McBride (1989), the midtropospheric peaks of apparent heat source in the Gulf of Carpentaria were approximately 23 K day^{-1} during the active period and approximately zero during the inactive period. Before examining the

PV cross-sections shown in the top panels of Figs. 1 and 2, let us briefly discuss the concept of Rossby-Ertel potential vorticity and its equivalent definitions in isobaric and isentropic coordinates.

The Rossby-Ertel potential vorticity can be calculated from observed pressure, temperature and winds using the quasi-static, isobaric coordinate form

$$P = \sigma_0 \Bigg\{ \frac{\partial v}{\partial p} \left(\frac{\partial \theta}{a \cos\phi \partial \lambda} \right)_p - \frac{\partial u}{\partial p} \left(\frac{\partial \theta}{a \partial \phi} \right)_p$$

$$- \left[2\Omega \sin\phi + \left(\frac{\partial v}{a \cos\phi \partial \lambda} \right)_p - \left(\frac{\partial (u \cos\phi)}{a \cos\phi \partial \phi} \right)_p \right] \frac{\partial \theta}{\partial p} \Bigg\}, \tag{2.1}$$

or the isentropic coordinate form

$$P = \frac{\sigma_0}{\sigma} \left[2\Omega \sin\phi + \left(\frac{\partial v}{a \cos\phi \partial \lambda} \right)_\theta - \left(\frac{\partial (u \cos\phi)}{a \cos\phi \partial \phi} \right)_\theta \right], \tag{2.2}$$

where $\sigma = -\partial p / \partial \theta$ is the isentropic pseudodensity and σ_0 is a constant reference value of σ. The forms (2.1) and (2.2) are equivalent, and it is a simple matter to transform from one to the other (e.g., the single term involving v in (2.2) transforms into the two terms involving v in (2.1), with the term involving $(\partial \theta / \partial \lambda)_p$ accounting for the fact that θ-surfaces and p-surfaces may not be parallel). Because the sum of terms in the square brackets of (2.1) is different than the sum of terms in the square brackets of (2.2), we shall use different terminology in reference to them, i.e., *isobaric absolute vorticity* for the sum of terms in the square brackets of (2.1) and *isentropic absolute vorticity* for the sum of terms in the square brackets of (2.2). However, since the total right hand side of (2.1) is equivalent to the total right hand side of (2.2), we shall refer to either of them as simply PV.†

For the sake of convenience, we shall use formula (2.1) when computing PV from the AMEX data and formula (2.2) in the theoretical analysis of section 3, but it should be noted that we are talking about the same physical quantity. In either case, equations (2.1) and (2.2) reflect our belief that potential vorticity is easier

† Because the adjective 'isentropic' is not a useful modifier of the noun 'potential vorticity', we shall avoid use of the term 'isentropic potential vorticity'. However, we note that the term 'isentropic potential vorticity map' (IPV map) is useful if the adjective 'isentropic' is taken to modify map rather than potential vorticity, i.e., if we interpret 'IPV map' as short for 'PV map on an isentropic surface.'

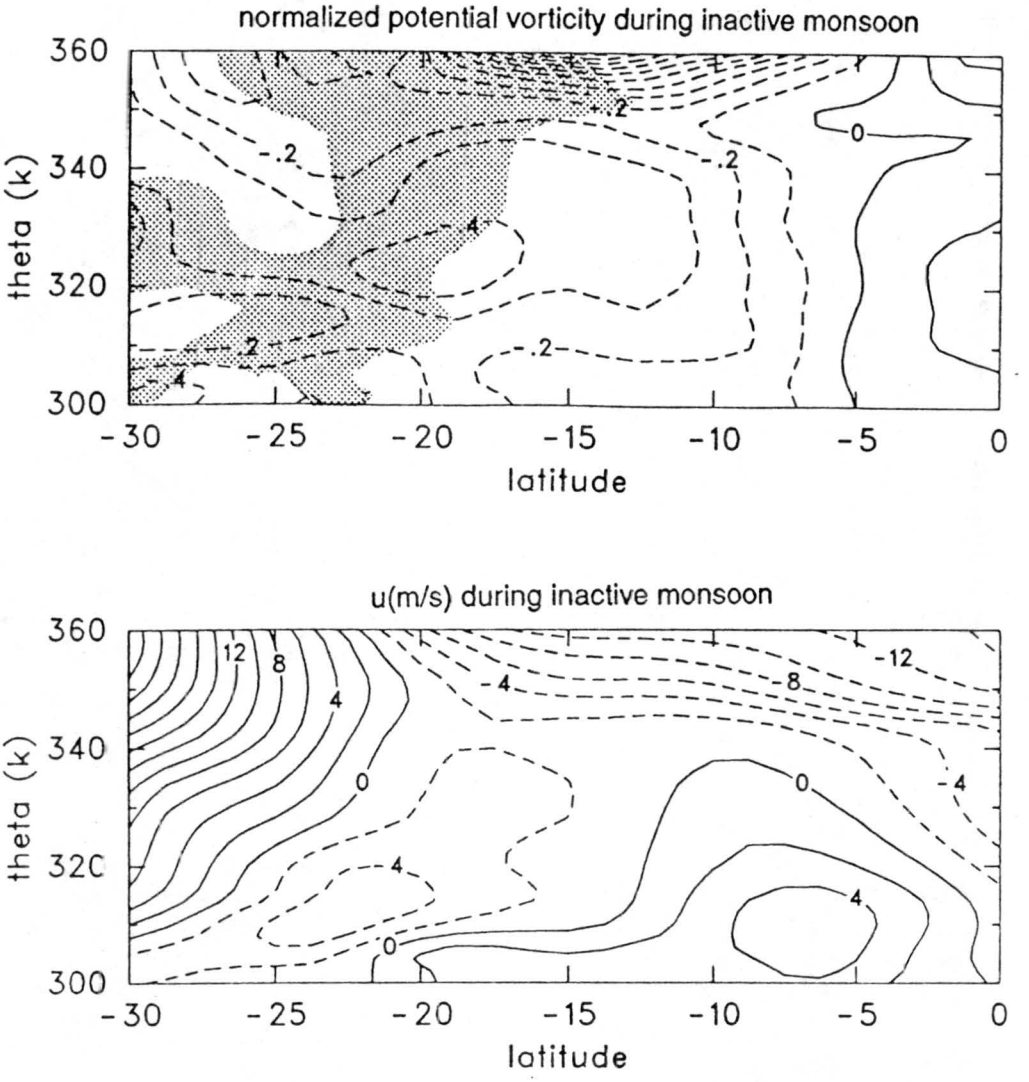

Figure 1. The top panel shows isolines of the dimensionless potential vorticity $P/(2\Omega)$ averaged over an area (110–135 E) and period (25–29 January 1987) of inactive monsoon during AMEX. The stippling indicates regions where the poleward isentropic gradient of potential vorticity is reversed. The bottom panel shows the zonal winds associated with the potential vorticity field. Solid lines indicate westerly flow and dashed lines easterly flow, with a contour interval of 2 ms^{-1}.

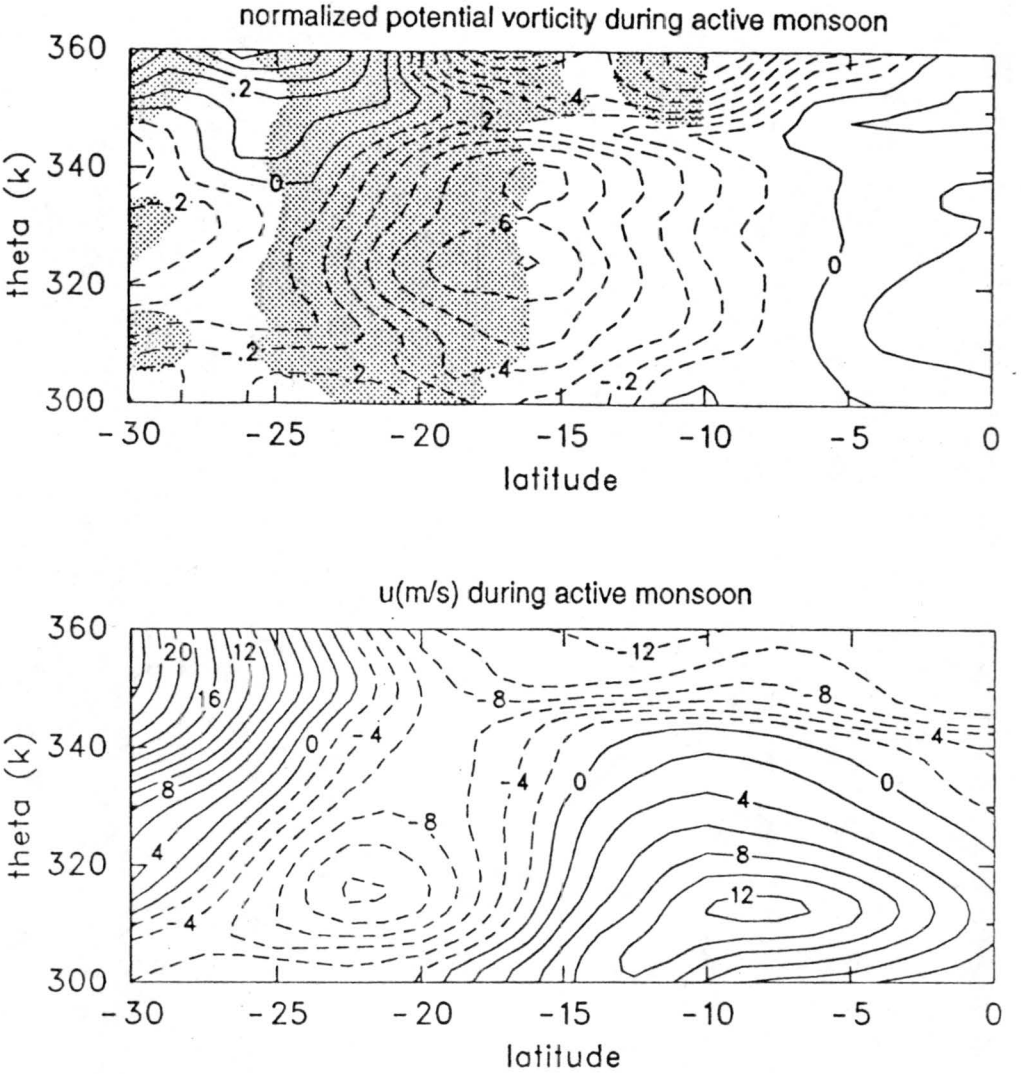

Figure 2. The top panel shows isolines of the dimensionless potential vorticity $P/(2\Omega)$ averaged over an area (110–135 E) and period (30 January to 4 February 1987) of intense convection during AMEX. The stippling indicates regions where the poleward isentropic gradient of potential vorticity is reversed. The bottom panel shows the zonal winds associated with the potential vorticity field. Solid lines indicate westerly flow and dashed lines easterly flow, with a contour interval of 2 ms^{-1}.

to interpret if we define it in such a way that it has the same units as vorticity. Thus, the introduction of the reference value σ_0 in (2.1) and (2.2) is analogous to the introduction of a reference pressure in the definition of potential temperature in order that it have the same units as temperature. For the observational and model results presented here we have chosen $\sigma_0 = 1458$ Pa K^{-1}. According to (2.2) the potential vorticity of an air parcel is equal to the isentropic absolute vorticity the air parcel would acquire under an adiabatic rearrangment which changed its actual pseudodensity σ to the constant reference value σ_0. With the definitions (2.1) and (2.2) it is natural to plot diagrams of the dimensionless quantity $P/(2\Omega)$. This partly overcomes the difficulty in interpretation caused by the rather obscure units associated with the usual definitions of potential vorticity.

The potential vorticity fields for the inactive and active periods are shown in Figs. 1 and 2. The main feature of interest is the large negative PV anomaly centered near 16 S and 325 K (550 mb) in the active period. The necessary condition for combined barotropic-baroclinic instability is met because south of this anomaly there is a large reversal in the PV gradient. During the active period the magnitude of this gradient is approximately five times larger than its value during the break period. A second area of PV gradient reversal is present equatorward of the ITCZ and at upper levels. These regions of reversed isentropic poleward gradient of PV are indicated by stippling in Figs. 1 and 2. Also present in this figure are regions where the necessary condition for inertial instability ($fP < 0$) is met. The first area where this condition is met lies between the equator and 5 S where air parcels from the northern hemisphere (with $P > 0$) have moved into the southern hemisphere. The second area lies on the anticyclonic side of the subtropical jet (i.e., poleward of 22 S and above 340 K). Whereas this latter area of instability does not appear in the mean PV field computed over the entire phase II AMEX period, the other areas mentioned here are present in the 37-day averaged field. In the next section we shall see to what extent these observed features can be reproduced by a zonally symmetric, inviscid, balanced model of the Hadley circulation.

3. Zonally symmetric balanced model

Using the potential temperature θ as the vertical coordinate, the equations for thermally forced, inviscid, zonally symmetric, balanced flow can be written

$$\frac{Du}{Dt} - \left(2\Omega \sin\phi + \frac{u \tan\phi}{a}\right) v = 0, \tag{3.1}$$

$$\left(2\Omega \sin\phi + \frac{u\tan\phi}{a}\right) u + \frac{\partial M}{a\partial\phi} = 0, \tag{3.2}$$

$$\frac{\partial M}{\partial\theta} = \Pi, \tag{3.3}$$

$$\frac{D\sigma}{Dt} + \sigma\left(\frac{\partial(v\cos\phi)}{a\cos\phi\partial\phi} + \frac{\partial\dot{\theta}}{\partial\theta}\right) = 0, \tag{3.4}$$

where

$$\frac{D}{Dt} = \frac{\partial}{\partial t} + v\frac{\partial}{a\partial\phi} + \dot{\theta}\frac{\partial}{\partial\theta} \tag{3.5}$$

is the total derivative, u and v the zonal and meridional components of the wind, $\Pi = c_p(p/p_0)^\kappa$ the Exner function, $M = \theta\Pi + gz$ the Montgomery potential, $\sigma = -\partial p/\partial\theta$ the pseudodensity in θ-space, and $\dot{\theta} = D\theta/Dt$ the effect of heating. Using the definitions of Π and σ, the set (3.1)–(3.4) can be considered closed in the unknowns u, v, p and M. However, it is not a convenient set for prediction since (3.1) and (3.4) cannot be used as independent predictors. In particular, the prediction of u by (3.1) and the prediction of p by (3.4) must be consistent with a continuous state of zonal wind and hydrostatic balance, as required by (3.2) and (3.3). This implies that only one dependent variable should be predicted. One possible choice for the predictive variable is the potential vorticity. The potential vorticity principle associated with the balanced set (3.1)–(3.4) can be derived by first noting that the equation for the *isentropic absolute vorticity* takes the form

$$\frac{D\zeta}{Dt} + \zeta\frac{\partial(v\cos\phi)}{a\cos\phi\partial\phi} - \frac{\partial u}{\partial\theta}\frac{\partial\dot{\theta}}{a\partial\phi} = 0, \tag{3.6}$$

where $\zeta = 2\Omega\sin\phi - \partial(u\cos\phi)/(a\cos\phi\partial\phi)$ is the zonally symmetric form of the isentropic absolute vorticity. Eliminating the isentropic divergence between (3.4) and (3.6) we obtain

$$\frac{\sigma}{\sigma_0}\frac{DP}{Dt} = \frac{\partial u}{\partial\theta}\frac{\partial\dot{\theta}}{a\partial\phi} + \zeta\frac{\partial\dot{\theta}}{\partial\theta}, \tag{3.7}$$

where $P = (\sigma_0/\sigma)\zeta$ is the potential vorticity [the zonally symmetric form of (2.2)]. This form of the potential vorticity equation will prove useful after we make a coordinate transformation which will simplify the total derivative operator.

The zonal momentum equation (3.1) can also be written in the absolute angular momentum form $D(\Omega a\cos^2\phi + u\cos\phi)/Dt = 0$. Since absolute angular momentum is conserved, one might expect certain advantages in using it as a coordinate in place of ϕ. We follow this general approach but, in particular, use as a new coordinate

the potential latitude Φ (Hack et al. 1989, Schubert et al. 1991), which is related to the actual latitude ϕ and the zonal wind u by $\Omega a \cos^2 \Phi = \Omega a \cos^2 \phi + u \cos \phi$. This relation allows the potential latitude to be interpreted as the latitude to which an air parcel must be moved (conserving absolute angular momentum) in order for its zonal wind component to vanish. Let us now consider (Φ, Θ, T) space, where $\Theta = \theta$ and $T = t$. The symbols Θ and T are introduced to distinguish partial derivatives at fixed ϕ ($\partial/\partial\theta$ and $\partial/\partial t$) from partial derivatives at fixed Φ ($\partial/\partial\Theta$ and $\partial/\partial T$). We can now easily show that (3.5) can also be written as

$$\frac{D}{Dt} = \frac{\partial}{\partial T} + \dot{\theta}\frac{\partial}{\partial \Theta}. \tag{3.8}$$

The advantage of (3.8) over (3.5) is the elimination of the divergent wind component v, which is now implicit in the coordinate transformation.

Let us now introduce the potential pseudodensity $\sigma^* = (2\Omega \sin \Phi/\zeta)\sigma$. The potential pseudodensity is related to the potential vorticity by $\sigma^* P = \sigma_0 2\Omega \sin \Phi$ and is simply the pseudodensity a parcel would acquire if ζ were changed to $2\Omega \sin \Phi$ under conservation of P. Since σ^* is proportional to P^{-1}, the potential pseudodensity equation can be easily obtained from the potential vorticity equation (3.7). To begin we note that $(\partial u/\partial\theta)(\partial/a\partial\phi) + \zeta(\partial/\partial\theta) = \zeta(\partial/\partial\Theta)$, which allows us to rewrite the right hand side of (3.8). Then, with D/Dt given by (3.8), the potential pseudodensity equation becomes

$$\frac{\partial \sigma^*}{\partial T} + \frac{\partial(\sigma^* \dot{\theta})}{\partial \Theta} = 0. \tag{3.9}$$

In the absence of heating, σ^* is invariant. The advantage of (3.9) is that, if the source term $\dot{\theta}$ is a known function of (Φ, Θ, T), then the problem of solving for the time evolution of σ^* has separated from the rest of the dynamics. If $\dot{\theta}$ is simple enough, (3.9) can even be solved analytically.

To solve (3.9) analytically let us consider the simple case in which $\dot{\theta}$ is independent of time and is given by

$$\dot{\theta}(S, Z) = Q(S) \begin{cases} 0 & \text{if } \lambda Z \geq \pi \\ \sin^2(\lambda Z) & \text{if } \lambda Z < \pi \end{cases} \tag{3.10a}$$

where

$$Q(S) = Q_0 4\alpha\pi^{-\frac{1}{2}} \left\{ \operatorname{erf}\left[\alpha(1+S_c)\right] + \operatorname{erf}\left[\alpha(1-S_c)\right] \right\}^{-1} \exp\left[-\alpha^2 (S - S_c)^2\right], \tag{3.10b}$$

$S = \sin\Phi$ and $Z = (\Theta - \Theta_B)/(\Theta_T - \Theta_B)$. By varying the parameters λ, S_c and α we can consider simulated ITCZ's with heating patterns centered at different heights and latitudes and with different extents in the vertical and horizontal. By integration of (3.10b) from the south pole to the north pole we can show that $\frac{1}{2}\int Q(S)\,dS = Q_0$, so that different values of S_c and α all result in the same area averaged heating Q_0. For the results shown here we have chosen $\alpha = 7.5$ and either $S_c = \sin(-10°) \approx -0.174$ or $S_c = \sin(-15°) \approx -0.259$. These can be interpreted as rather broad ITCZ's with approximately 85% of their rainfall occurring within a fifteen degree latitude band centered on 10 S or 15 S. From (3.10) and the predictive equation (3.9) we find that

$$\frac{\partial\sigma^*}{\partial\tau} = 0 \qquad \text{if} \quad \lambda Z \geq \pi, \tag{3.11a}$$

$$\frac{\partial(\dot{\theta}\sigma^*)}{\partial\tau} + \sin^2(\lambda Z)\frac{\partial(\dot{\theta}\sigma^*)}{\partial Z} = 0 \qquad \text{if} \quad \lambda Z < \pi, \tag{3.11b}$$

where $\tau(S) = Q(S)T/(\Theta_T - \Theta_B)$ is the dimensionless "convective clock" time. According to (3.11b) the quantity $\dot{\theta}\sigma^*$ is constant along each characteristic curve determined from $dZ/\sin^2(\lambda Z) = d\tau$. By integration of this equation we can show that the characteristic through the point (Z,τ) intersects the $\tau = 0$ axis at a level $Z_0(Z,\tau)$ determined by

$$\lambda Z_0 = \begin{cases} \lambda Z & \text{if } \lambda Z \geq \pi, \\ \cot^{-1}\left[\cot(\lambda Z) + \lambda\tau\right] & \text{if } \lambda Z < \pi. \end{cases} \tag{3.12}$$

Since $\dot{\theta}\sigma^*$ is constant along each characteristic, its value at (Z,τ) must equal its value at $(Z_0(Z,\tau),0)$, which results in

$$\sigma^*(Z,\tau) = \sigma^*(Z_0,0)\frac{\sin^2(\lambda Z_0)}{\sin^2(\lambda Z)}. \tag{3.13}$$

The analytic solution (3.13) constitutes an *internal* potential pseudodensity anomaly, i.e., a σ^* field which is modified at $0 < \lambda Z < \pi$. For the results presented here we have specified $\Theta_T = 360$ K, $\Theta_B = 300$ K and $\lambda = 1.1\pi$, which places the top of the heating at $\sim$ 150mb. Because of the way the product $Q(S)T$ appears in (3.11b) it is not really necessary to choose Q_0; rather, the solution can simply be obtained for different values of Q_0T. However, for purposes of physical interpretation let us choose $Q_0 = 1.5$ K day^{-1}. Then, the peak heating is $Q(S_c) \approx 12.5$ K day^{-1} and $T = 2$ days corresponds to $Q_0T = 3.0$ K. For the results presented here we have

specified an initial σ^* which depends on θ but not on ϕ. This represents an initial state with no zonal flow and with a mean tropical temperature profile. The mean tropical temperature profile is taken from the sector average temperature at 12.5S for the disturbed AMEX period presented in Fig. 2.

Now that σ^* has been determined analytically, our final theoretical task is to determine both the wind and mass fields from the σ^* field. This task can be accomplished because the definition of σ^*, along with the gradient and hydrostatic constraints, lead to a coupled pair of equations which relate the known σ^* field to the unknown $\mathcal{M} = M + \frac{1}{2}u^2$ and $\sin\phi$ fields. We shall refer to this pair of equations and its associated boundary conditions as the invertibility principle. To derive the invertibility principle we use the definition of σ^* to obtain the Jacobian form $\partial(s,p)/\partial(S,\Theta) + \sigma^* = 0$, where $s = \sin\phi$. Using the transformed hydrostatic equation $\partial\mathcal{M}/\partial\Theta = \Pi$ we can write this Jacobian form and the zonal balance condition as

$$\frac{\partial s}{\partial S}\frac{\partial^2\mathcal{M}}{\partial\Theta^2} - \frac{\partial s}{\partial\Theta}\frac{\partial^2\mathcal{M}}{\partial S\partial\Theta} + \Gamma\sigma^* = 0, \tag{3.14a}$$

$$2\Omega^2 a^2 S\left(\frac{s^2 - S^2}{1 - s^2}\right) + \frac{\partial\mathcal{M}}{\partial S} = 0, \tag{3.14b}$$

where $\Gamma = \kappa\Pi/p$. Equations (3.14a–b) constitute the desired relation between $\mathcal{M}$, s and σ^*. For boundary conditions we choose

$$\frac{\partial\mathcal{M}}{\partial\Theta} = \Pi_T \quad \text{at} \quad \Theta = \Theta_T, \tag{3.14c}$$

$$\Theta\frac{\partial\mathcal{M}}{\partial\Theta} - \mathcal{M} + \frac{\Omega^2 a^2(s^2 - S^2)^2}{2(1 - s^2)} = 0 \quad \text{at} \quad \Theta = \Theta_B, \tag{3.14d}$$

$$s = 1 \quad \text{at} \quad S = 1, \tag{3.14e}$$

$$s = -1 \quad \text{at} \quad S = -1. \tag{3.14f}$$

Equation (3.14c) results from assuming that the upper isentropic surface $\Theta = \Theta_T$ is also an isobaric surface with Exner function Π_T. The lower boundary condition results from assuming the geopotential vanishes on the lower isentropic surface $\Theta = \Theta_B$, so that $M = \Theta\Pi$ there. Then, expressing M in terms of $\mathcal{M}$ and s, we can write the lower boundary condition as (3.14d). For the boundary conditions at the poles, symmetry requires the conditions (3.14e,f).

We can now summarize the results of our analysis as follows. Since the time evolution of the σ^* field is determined from (3.13), we can then solve the diagnostic

problem (3.14) for $\mathcal{M}$ and s, after which u, Π and p are easily determined. This is all accomplished in (S, Θ) space. The transformation to other representations, e.g. $u(\phi, \theta)$ or $u(\phi, p)$, is straightforward.

For the case of an ITCZ at 15 S the fields of σ^*, P and u at 2 days are shown in Fig. 3. In the ITCZ a region of negative potential vorticity develops at low and mid-levels. The solution of the invertibility principle results in low level zonal flows which are easterly except in a band which runs between a latitude just south of the equator and a latitude near the center of the ITCZ. At upper levels the zonal flow is westerly except in a band which runs between a latitude just north of the equator and a latitude near the center of the ITCZ. These modeled winds contain all the major features of the observed zonal winds shown in Fig. 2, except for the subtropical jet whose origin is beyond the model's physics.

The convective modification of the P field occurs within a background state which has a northward increase of P. As convection continues the gradient of P becomes locally reversed in the lower troposphere poleward of the ITCZ and in the upper troposphere equatorward of the ITCZ. These regions of reversed isentropic poleward gradient of potential vorticity are indicated by stippling in Fig. 3. Such features develop quickly and are consistent with observations made by Burpee (1972) and Reed et al. (1977) in their studies of the origins of easterly waves in the lower troposphere of the north African region. According to Charney and Stern (1962) and Eliassen (1983), such zonal flows (i.e., those with a reversal in the meridional gradient of the potential vorticity) satisfy the necessary condition for combined barotropic-baroclinic instability. Thus, it would appear that ITCZ convection alone can lead to the generation of unstable zonal flows. This may be the cause of periodic breakdowns of the ITCZ. The precise role of the upper level potential vorticity gradient reversal remains intriguing.

Results at 2 days for an ITCZ located at 10 S are shown in Fig. 4. Comparing Fig. 4 with Fig. 3 we note that, except for the latitudinal shift, the σ^* fields are essentially identical. However, the potential vorticity, zonal wind and mass fields are different, with the ITCZ at 15 S producing a potential vorticity anomaly, neighboring zonal winds and isobaric surface deviations noticeably larger than those produced by the ITCZ at 10 S. These differences can be interpreted as follows. Since $D\sigma^*/Dt = -\sigma^* \partial\dot{\theta}/\partial\Theta$ and the initial σ^* is independent of latitude, the time evolution of σ^* for ITCZ's at different latitudes is essentially identical except for the meridional shift. Since $DP/Dt = P\partial\dot{\theta}/\partial\Theta$ and the initial magnitude of P is larger at 15 S, the material rate of change of P is also larger for an ITCZ at this latitude.

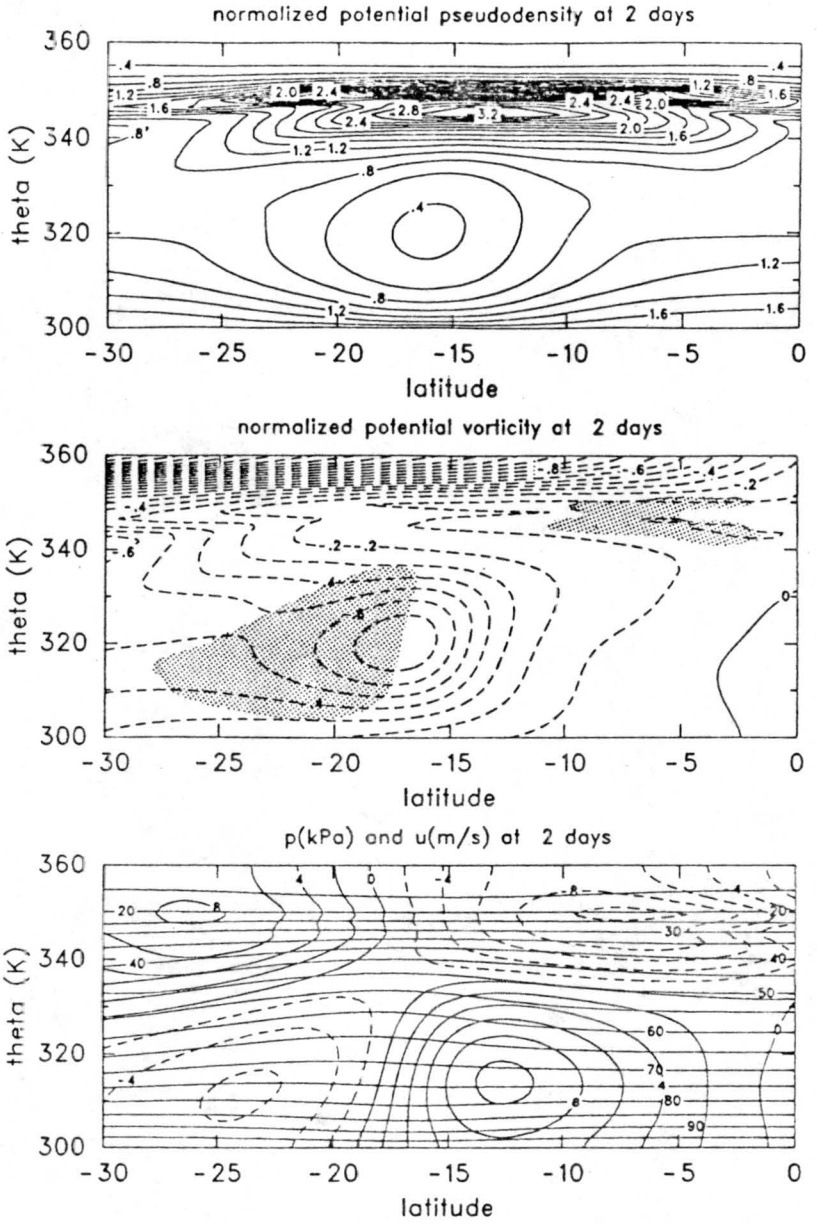

Figure 3. Model results at $T = 2$ days for an ITCZ located at 15 S. The top panel shows isolines of σ^*/σ_0 (i.e., potential pseudodensity measured in units of σ_0) in (ϕ, θ) space. Note that the convection of the ITCZ generates a lower tropospheric region of low potential pseudodensity and an upper tropospheric region of high potential pseudodensity. The middle panel shows isolines of $P/(2\Omega)$ (i.e., potential vorticity measured in units of 2Ω). The stippling indicates regions where the poleward isentropic gradient of potential vorticity is reversed. The bottom panel shows pressure (nearly horizontal lines) in kPa and zonal balanced wind in ms^{-1}. Solid wind contours indicate westerly flow, dashed contours easterly flow, with a contour interval of 2 ms^{-1}. These wind and mass fields are in (ϕ, θ) space and are associated with the potential pseudodensity and potential vorticity fields shown in the upper two panels.

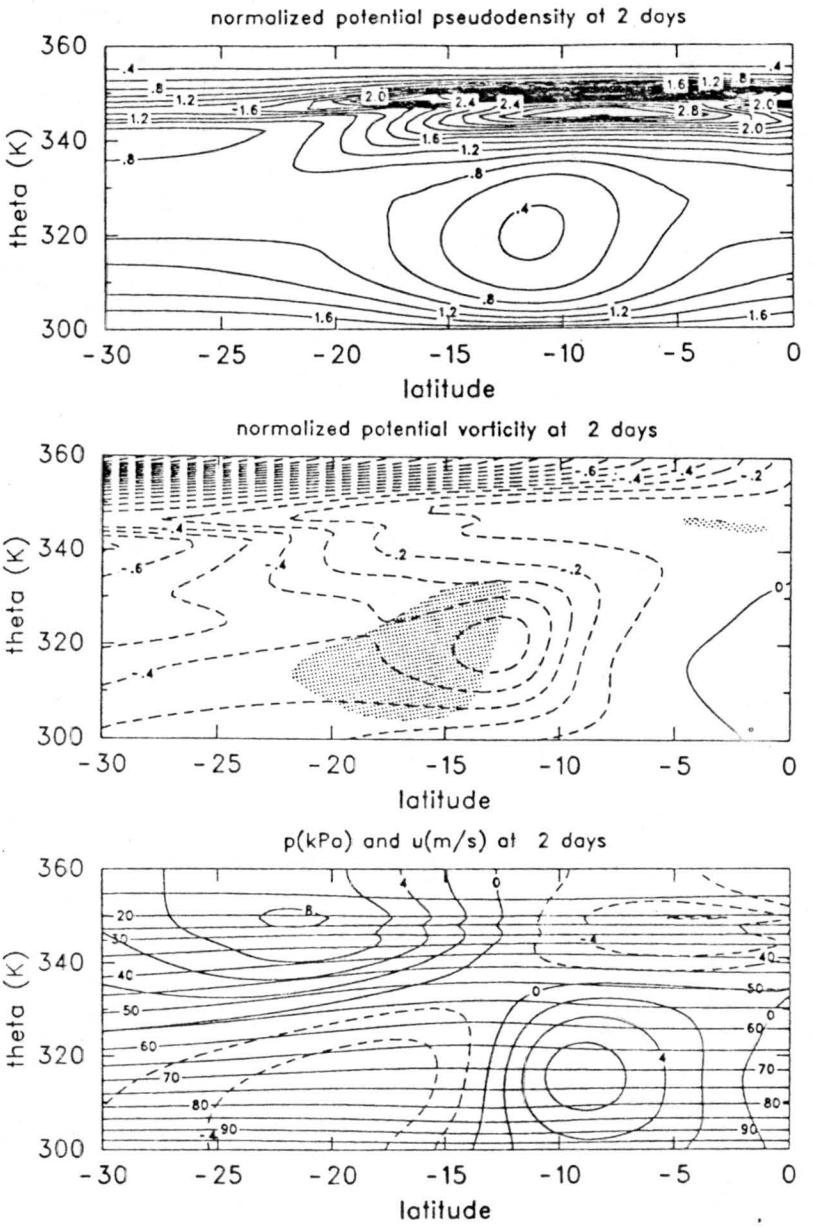

Figure 4. As in Fig. 3 but for an ITCZ at 10 S.

An alternate interpretation is that, since $P = (\sigma_0/\sigma^*)2\Omega \sin \Phi$, shifted but otherwise identical σ^* anomalies result in P anomalies which are approximately 50% larger for the ITCZ at 15 S.

4. Nondivergent barotropic instability of the monsoon trough shear zone

The potential vorticity gradient reversal at lower tropospheric levels on the poleward side of the ITCZ sets the stage for combined barotropic-baroclinic instability. Since the potential vorticity field near the ITCZ is induced by moist physical processes, we would expect these same moist processes, along with barotropic and baroclinic instability effects, to play a role in the evolution of wave disturbances developing out of this background state. Apparently, barotropic processes play a particularly important role. To isolate these processes, we shall first consider the nondivergent barotropic model. In the following two subsections we consider both the linear and nonlinear stability conditions.

a. sufficient condition for linear stability

Let us first consider the nondivergent barotropic vorticity equation linearized about a basic state zonal flow $\bar{u}$ which varies with latitude. This equation takes the form

$$\frac{\partial \zeta'}{\partial t} + \bar{u}\frac{\partial \zeta'}{a\cos\phi \partial \lambda} + v'\frac{d\bar{\zeta}}{a d\phi} = 0, \tag{4.1}$$

where

$$\bar{\zeta} = 2\Omega \sin\phi - \frac{\partial(\bar{u}\cos\phi)}{a\cos\phi\partial\phi}, \quad \zeta' = \frac{\partial v'}{a\cos\phi\partial\lambda} - \frac{\partial(u'\cos\phi)}{a\cos\phi\partial\phi}, \tag{4.2a, b}$$

and the perturbation wind components (u', v') satisfy the nondivergent relation

$$\frac{\partial u'}{a\cos\phi\partial\lambda} + \frac{\partial(v'\cos\phi)}{a\cos\phi\partial\phi} = 0. \tag{4.3}$$

Defining $\mathcal{D}/\mathcal{D}t$ as the derivative following the basic state zonal flow, the first two terms in (4.1) can be written $\mathcal{D}\zeta'/\mathcal{D}t$. Defining the meridional particle displacement η by $\mathcal{D}\eta/\mathcal{D}t = v'$, we can integrate (4.1) to obtain

$$\zeta' + \frac{d\bar{\zeta}}{a d\mu}\eta\cos\phi = 0, \tag{4.4}$$

where $\mu = \sin\phi$. Multiplying (4.4) by $v' \cos\phi$ we obtain

$$\frac{\mathcal{D}A}{\mathcal{D}t} = -v'\zeta' \cos\phi, \quad \text{where} \quad A = \frac{d\bar{\zeta}}{ad\mu} \tfrac{1}{2}\eta^2 \cos^2\phi = \left(\frac{d\bar{\zeta}}{ad\mu}\right)^{-1} \tfrac{1}{2}\zeta'^2 \qquad (4.5a, b)$$

is the wave-activity. Using (4.2b) and the condition of nondivergence in the right hand side of (4.5a), we can rearrange the wave-activity equation into the form

$$\frac{\partial A}{\partial t} + \frac{\partial \left[\bar{u}A + \frac{1}{2}(v'^2 - u'^2)\cos\phi\right]}{a\cos\phi\partial\lambda} + \frac{\partial \left[-u'v'\cos^2\phi\right]}{a\cos\phi\partial\phi} = 0. \qquad (4.6)$$

Finally, integration of (4.6) over the sphere yields

$$\frac{d}{dt}\iint A\, d\lambda d\mu = 0. \qquad (4.7)$$

Since the integral in (4.7) must be constant in time, (4.5b) shows that if $\bar{\zeta}$ is a monotonically increasing function of μ, neither η^2 nor ζ'^2 can grow in an overall sense. Thus, a necessary condition for instability is that $d\bar{\zeta}/d\mu$ have both signs. For the AMEX observations shown in Fig. 2 and for the model results shown in Figs. 3 and 4 this condition is met because of the reversal of the poleward gradient of potential vorticity (and hence also isentropic absolute vorticity) on the south side of the ITCZ.

The simple linear barotropic argument given above can be generalized in several ways. Baroclinic effects can be included in both the quasigeostrophic (Charney and Stern 1962) and semigeostrophic (Eliassen 1983, Magnusdottir and Schubert 1990, 1991) frameworks. In addition the analysis need not be limited to parallel shear flows (Andrews 1983) or even to linearized dynamics (Arnol'd 1965, 1966; Drazin and Reid 1981; McIntyre and Shepherd 1987; Shepherd 1988a,b, 1989, 1990). It is the nonlinear extension which we shall now consider.

b. sufficient condition for nonlinear stability

In order to generalize the linear arguments of the previous subsection, we now begin with the nonlinear barotropic vorticity equation

$$\frac{D\zeta}{Dt} = \frac{\partial\zeta}{\partial t} + u\frac{\partial\zeta}{a\cos\phi\partial\lambda} + v\frac{\partial\zeta}{a\partial\phi} = 0, \qquad (4.8)$$

where

$$\zeta = 2\Omega\sin\phi + \frac{\partial v}{a\cos\phi\partial\lambda} - \frac{\partial(u\cos\phi)}{a\cos\phi\partial\phi} \qquad (4.9)$$

is the absolute vorticity and the nondivergent wind components (u, v) satisfy the continuity equation

$$\frac{\partial u}{a\cos\phi\partial\lambda} + \frac{\partial(v\cos\phi)}{a\cos\phi\partial\phi} = 0. \tag{4.10}$$

We now divide the fields into basic state parts and parts associated with waves or eddies, e.g., $\zeta(\lambda,\mu,t) = \bar{\zeta}(\mu) + \zeta'(\lambda,\mu,t)$, where $\bar{(\ )}$ denotes the basic state part and $(\ )'$ the departure from the basic state. No linearization will be performed so that the primed variables are not necessarily small amplitude. The λ-invariant basic state flow is assumed to be a steady solution of (4.8). We consider the case in which $\bar{\zeta}(\mu)$ is a monotonically increasing function of μ, and thereby define the inverse function $\bar{\mu}(\zeta)$ such that $\bar{\mu}(\bar{\zeta}(\mu)) = \mu$. Then, differentiating this last expression with respect to μ, we obtain $\bar{\mu}_\zeta \bar{\zeta}_\mu = 1$.

As the nonlinear generalization of the small amplitude wave-activity (4.5b), we now follow McIntyre and Shepherd (1987), Shepherd (1988a) and Haynes (1988) to define

$$A(\bar{\zeta},\zeta') = a\int_0^{\zeta'} \left[\bar{\mu}(\bar{\zeta}+\tilde{\zeta}) - \bar{\mu}(\bar{\zeta})\right] d\tilde{\zeta}. \tag{4.11}$$

If we approximate $\bar{\mu}(\bar{\zeta}+\tilde{\zeta})$ in (4.11) by the first two terms in a Taylor series expansion about $\bar{\zeta}$, it is easily shown that (4.11) reduces to (4.5b). To derive the equation obeyed by $A(\bar{\zeta},\zeta')$ we first take the total derivative of this finite amplitude wave activity to obtain

$$\frac{DA}{Dt} = \frac{\partial A}{\partial\bar{\zeta}}\frac{D\bar{\zeta}}{Dt} + \frac{\partial A}{\partial\zeta'}\frac{D\zeta'}{Dt}, \tag{4.12}$$

where, from (4.11),

$$\frac{\partial A}{\partial\bar{\zeta}} = a\left[\bar{\mu}(\bar{\zeta}+\zeta') - \bar{\mu}(\bar{\zeta}) - \bar{\mu}_\zeta(\bar{\zeta})\zeta'\right], \tag{4.13}$$

$$\frac{\partial A}{\partial\zeta'} = a\left[\bar{\mu}(\bar{\zeta}+\zeta') - \bar{\mu}(\bar{\zeta})\right]. \tag{4.14}$$

Equations (4.13) and (4.14), together with the fact that $-D\zeta'/Dt = D\bar{\zeta}/Dt = v'\partial\bar{\zeta}/a\partial\phi$, allow (4.12) to be written as

$$\frac{DA}{Dt} = -v'\zeta'\cos\phi, \tag{4.15}$$

which is a nonlinear generalization of (4.5a). Using the nondivergence condition (4.10), we can rewrite (4.15) in the flux form

$$\frac{\partial A}{\partial t} - \frac{\partial\left[uA + \frac{1}{2}(v'^2 - u'^2)\cos\phi\right]}{a\cos\phi\partial\lambda} + \frac{\partial\left[(vA - u'v'\cos\phi)\cos\phi\right]}{a\cos\phi\partial\phi} = 0. \tag{4.16}$$

Equation (4.16) is the finite amplitude wave-activity relation and is a generalization of the small amplitude relation (4.6). Several differences are noteworthy. All the primed quantities in (4.6) are small amplitude, whereas the primed quantities in (4.16) may be of finite amplitude. Where the flux (uA, vA) appears in the finite amplitude relation (4.16), the flux $(\bar{u}A, 0)$ appears in the small amplitude relation (4.6). Finally, the finite amplitude wave-activity is defined by (4.11), whereas the small amplitude wave-activity is defined by (4.5b).

To obtain the nonlinear stability condition we now integrate (4.16) over the surface of the sphere to obtain

$$\frac{d}{dt} \iint A d\lambda d\mu = 0. \tag{4.17}$$

Although this looks identical to (4.7), we must keep in mind that the A in (4.17) is defined by (4.11) while the A in (4.7) is defined by (4.5b). The results are consistent since (4.11) reduces to (4.5b) in the small amplitude limit. From the definition (4.11), we now note that

$$\frac{a\frac{1}{2}\zeta'^2}{|\bar{\zeta}_\mu|_{\max}} = a\int_0^{\zeta'} |\bar{\mu}_\zeta(\bar{\zeta})|_{\min}\tilde{\zeta}d\tilde{\zeta} \leq |A(\bar{\zeta},\zeta')| \leq a\int_0^{\zeta'} |\bar{\mu}_\zeta(\bar{\zeta})|_{\max}\tilde{\zeta}d\tilde{\zeta} = \frac{a\frac{1}{2}\zeta'^2}{|\bar{\zeta}_\mu|_{\min}}. \tag{4.18}$$

Together, (4.17) and (4.18) imply that

$$\frac{a}{|\bar{\zeta}_\mu|_{\max}} \iint \zeta'^2(\lambda,\mu,t)d\lambda d\mu \leq \iint A(\bar{\zeta},\zeta',t)d\lambda d\mu$$

$$= \iint A(\bar{\zeta},\zeta',0)d\lambda d\mu \leq \frac{a}{|\bar{\zeta}_\mu|_{\min}} \iint \zeta'^2(\lambda,\mu,0)d\lambda d\mu,$$

which can also be written

$$\iint \zeta'^2(\lambda,\mu,t)d\lambda d\mu \leq \frac{|\bar{\zeta}_\mu|_{\max}}{|\bar{\zeta}_\mu|_{\min}} \iint \zeta'^2(\lambda,\mu,0)d\lambda d\mu. \tag{4.19}$$

This is the form of Arnol'd's (1965, 1966) result derived by McIntyre and Shepherd (1987) and used by Shepherd (1988a) to obtain rigorous bounds on the nonlinear saturation of barotropic instabilities to parallel shear flows. The inequality (4.19) bounds the disturbance enstrophy at time t in terms of the initial disturbance enstrophy and the poleward gradient of the basic state absolute vorticity. It rules out the possibility of instability for basic state flows with $\bar{\zeta}_\mu > 0$ everywhere.

c. jets and shear layers

To actually confirm that a zonal flow is unstable and to find the growth rates and modes of breakdown of the flow, an eigenvalue-eigenfunction calculation is useful. At this point we introduce the β-plane approximation so that (4.1) simplifies to

$$\left(\frac{\partial}{\partial t} + \bar{u}\frac{\partial}{\partial x}\right)\nabla^2\psi + \frac{\partial\psi}{\partial x}\frac{d\bar{\zeta}}{dy} = 0, \tag{4.20}$$

where $\bar{\zeta}(y) = f_0 + \beta y - \bar{u}_y$ and ψ is the streamfunction for the perturbation horizontal velocity components $u' = -\partial\psi/\partial y$ and $v' = \partial\psi/\partial x$, in which case the perturbation vorticity is $\nabla^2\psi$. We shall search for solutions of (4.20) having the form $\psi(x,y,t) = \Psi(y)e^{ik(x-ct)}$ where k is the zonal wavenumber and c can be complex. Equation (4.20) then becomes

$$\frac{d^2\Psi}{dy^2} + \left(\frac{\beta - \bar{u}_{yy}}{\bar{u} - c} - k^2\right)\Psi = 0. \tag{4.21}$$

In discussions of barotropically unstable solutions of (4.21) it is common to consider two idealized types of basic flows—jets and shear layers. There are many studies of the generation of easterly waves from zonal jets (e.g., Nitta and Yanai 1969, Yamasaki and Wada 1972, Rennick 1976, Simmons 1977, Mass 1979, Williams et al. 1984, Peng and Williams 1986). One of the most extensively studied jets is the Bickley jet, for which

$$\bar{u}(y) = U\mathrm{sech}^2(y/y_0), \qquad \bar{\zeta}(y) = f_0 + \beta y + (2U/y_0)\mathrm{sech}^2(y/y_0)\tanh(y/y_0),$$

so that the poleward gradient of absolute vorticity is

$$\bar{\zeta}_y = \beta - \bar{u}_{yy} = \beta\left\{1 + (2/b)\mathrm{sech}^2(y/y_0)\left[1 - 3\tanh^2(y/y_0)\right]\right\},$$

where U and y_0 are specified constants and $b = \beta y_0^2/U$. Profiles of $\bar{u}$, $\bar{\zeta}$ and $\bar{\zeta}_y$ for both the westerly and easterly Bickley jets are shown in Fig. 5. One further differentiation of $\bar{\zeta}_y$ leads to the result that $\bar{\zeta}_y$ reaches its extrema at $\tanh(y/y_0) = \pm\sqrt{2/3}$ and $y = 0$. Requiring $\bar{\zeta}_y < 0$ at the minima leads to the necessary condition $-2 < b < 2/3$ for instability of the Bickley jet. Thus, we should expect more unstable states as y_0 decreases and $|U|$ increases. The necessary condition for the Bickley jet also suggests a difference between easterly ($b < 0$) and westerly ($b > 0$) jets, and detailed eigenvalue calculations (Kuo 1973, Fig. 7, or Haltiner and Williams 1980, Fig. 4.3) do indeed show that easterly Bickley jets are more unstable than corresponding westerly Bickley jets. Thus, if the easterly jet poleward of the

ITCZ and the westerly jet equatorward of the ITCZ are of equal strengths and equal widths, the easterly jet should be expected to be more dynamically active. An important argument against the use of the Bickley jet as an idealization of the easterly jet produced by the Hadley circulation is the position of the region of reversed absolute vorticity gradient. For the easterly Bickley jet this region is in the center of the jet (Fig. 5) while for monsoon type flows produced by ITCZ convection it lies equatorward of the easterly jet (Fig. 4). In this sense, idealized shear layer profiles may be more germane.

A useful idealization of the lower tropospheric monsoon trough shear zone of Figs. 3 and 4 is the hyperbolic tangent basic state, for which

$$\bar{u}(y) = U\tanh(y/y_0), \qquad \bar{\zeta}(y) = f_0 + \beta y - (U/y_0)\mathrm{sech}^2(y/y_0),$$

so that the poleward gradient of absolute vorticity is

$$\bar{\zeta}_y = \beta - \bar{u}_{yy} = \beta\left[1 + (2/b)\mathrm{sech}^2(y/y_0)\tanh(y/y_0)\right],$$

where again U and y_0 are specified constants and $b = \beta y_0^2/U$. Profiles of $\bar{u}$, $\bar{\zeta}$ and $\bar{\zeta}_y$ for this shear layer are shown in Fig. 6. One further differentiation of $\bar{\zeta}_y$ leads to the result that $\bar{\zeta}_y$ reaches its extreme values where $\tanh(y/y_0) = \pm\sqrt{1/3}$. At the extremum on the poleward (south) side of the ITCZ we have $\beta - \bar{u}_{yy} = \beta\left[1 - 4/(3\sqrt{3}b)\right]$. Thus, $\beta - \bar{u}_{yy}$ has both signs and the necessary condition for instability is satisfied if $|b| < 4/(3\sqrt{3}) \approx 0.77$. Again, we should expect more unstable states as y_0 decreases and $|U|$ increases. Note that ITCZ convection tends to push the atmosphere into a barotropically unstable state by decreasing b both through an increase in U and a decrease in y_0 (nonlinear collapse).

When the hyperbolic tangent wind field is used in (4.21) we obtain

$$\frac{d^2\Psi}{d\hat{y}^2} = \left[(ky_0)^2 - \frac{b + \mathrm{sech}^2\hat{y}\tanh\hat{y}}{\tanh\hat{y} - c/U}\right]\Psi, \tag{4.22}$$

where $\hat{y} = y/y_0$. With appropriate boundary conditions and for given ky_0 and b, this is an eigenvalue-eigenfunction problem for the complex eigenvalue c/U and the eigenfunction Ψ. Unfortunately, this problem cannot be solved analytically. Numerical solutions have been obtained for the nonrotating case by Michalke (1964) and for the rotating case by Lipps (1970), Williams et al. (1971), Dickinson and Clare (1973) and Kuo (1973). Kuo's results for the dimensionless growth rate $kc_i/(\beta y_0)$ as a function of ky_0 and b are shown in Fig. 7. Note that the growth rate

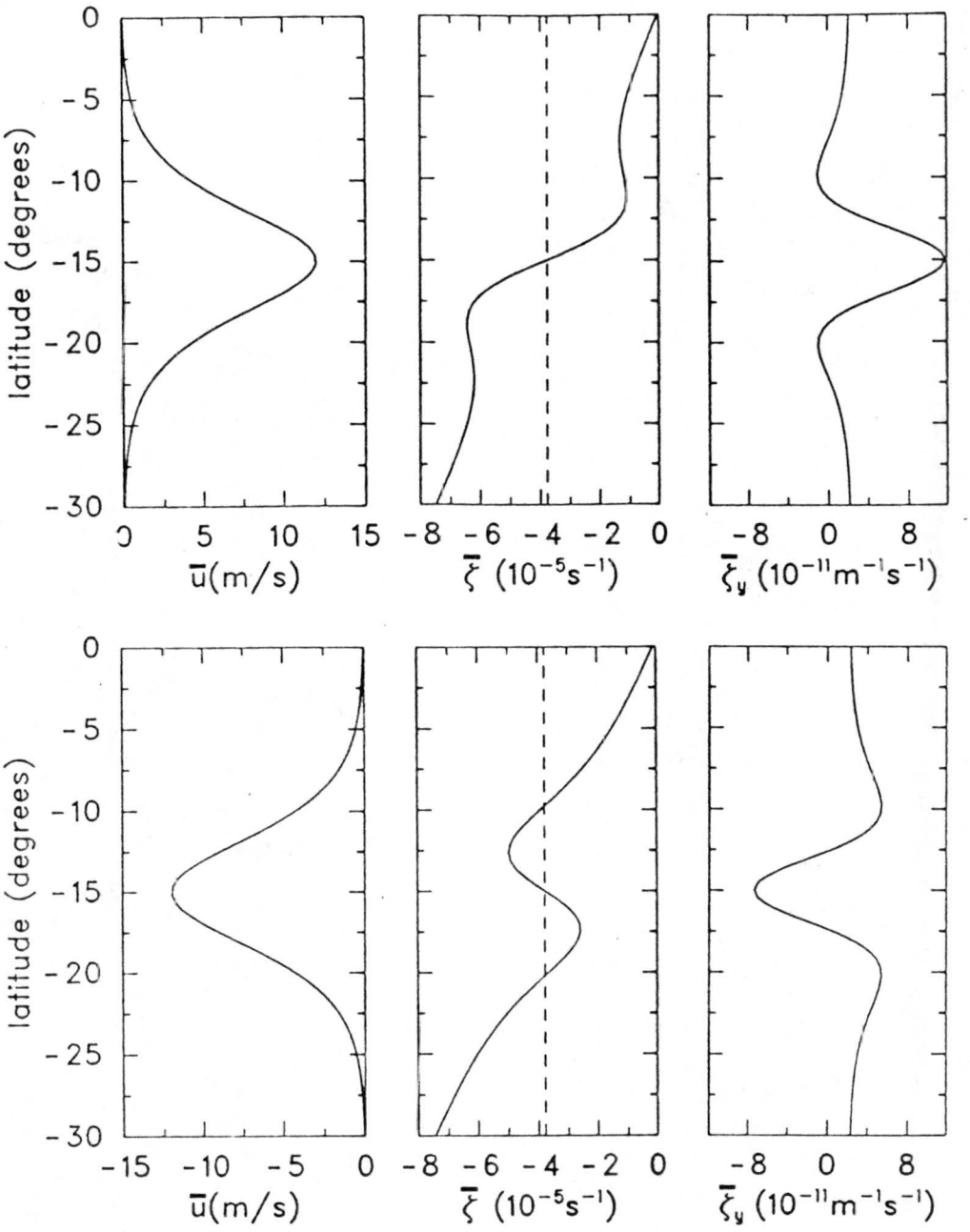

Figure 5. Top panels show profiles of $\bar{u}$, $\bar{\zeta}$ and f_0 (dashed), and $\bar{\zeta}_y$ for the westerly Bickley jet. Bottom panels show the same fields for the easterly Bickley jet. Note that the regions of reversed vorticity gradient are on the sides of the westerly Bickley jet but in the center of the easterly Bickley jet.

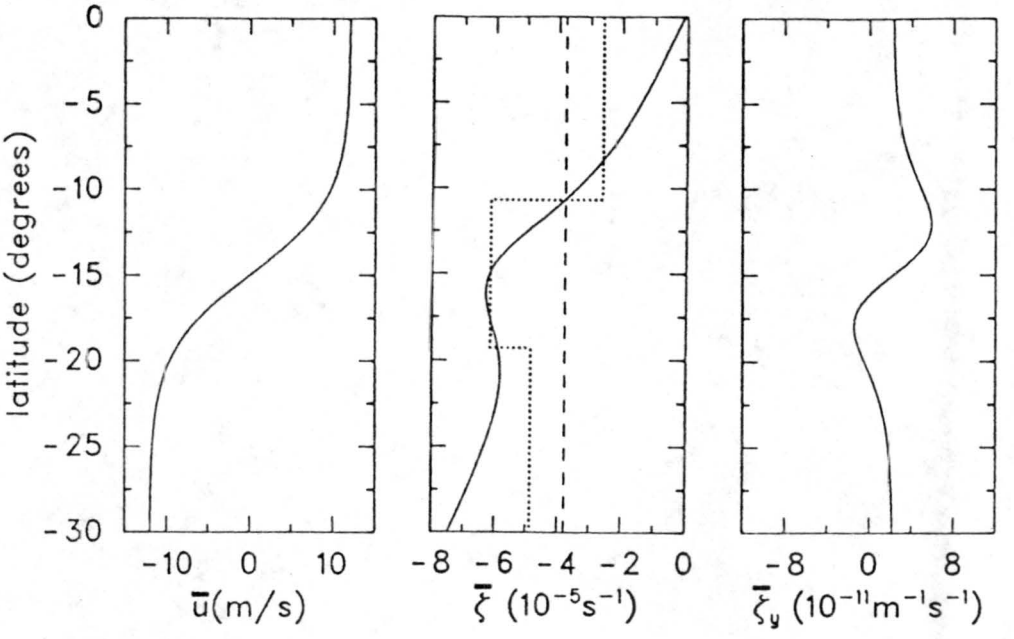

Figure 6. The three panels show profiles of $\bar{u}$, $\bar{\zeta}$ and f_0 (dashed), and $\bar{\zeta}_y$ for the hyperbolic tangent shear layer. The dotted line in the middle panel represents the $\bar{\zeta}$ profile for the three region model, which is meant to be an idealization of $\bar{\zeta}$ from the hyperbolic tangent case.

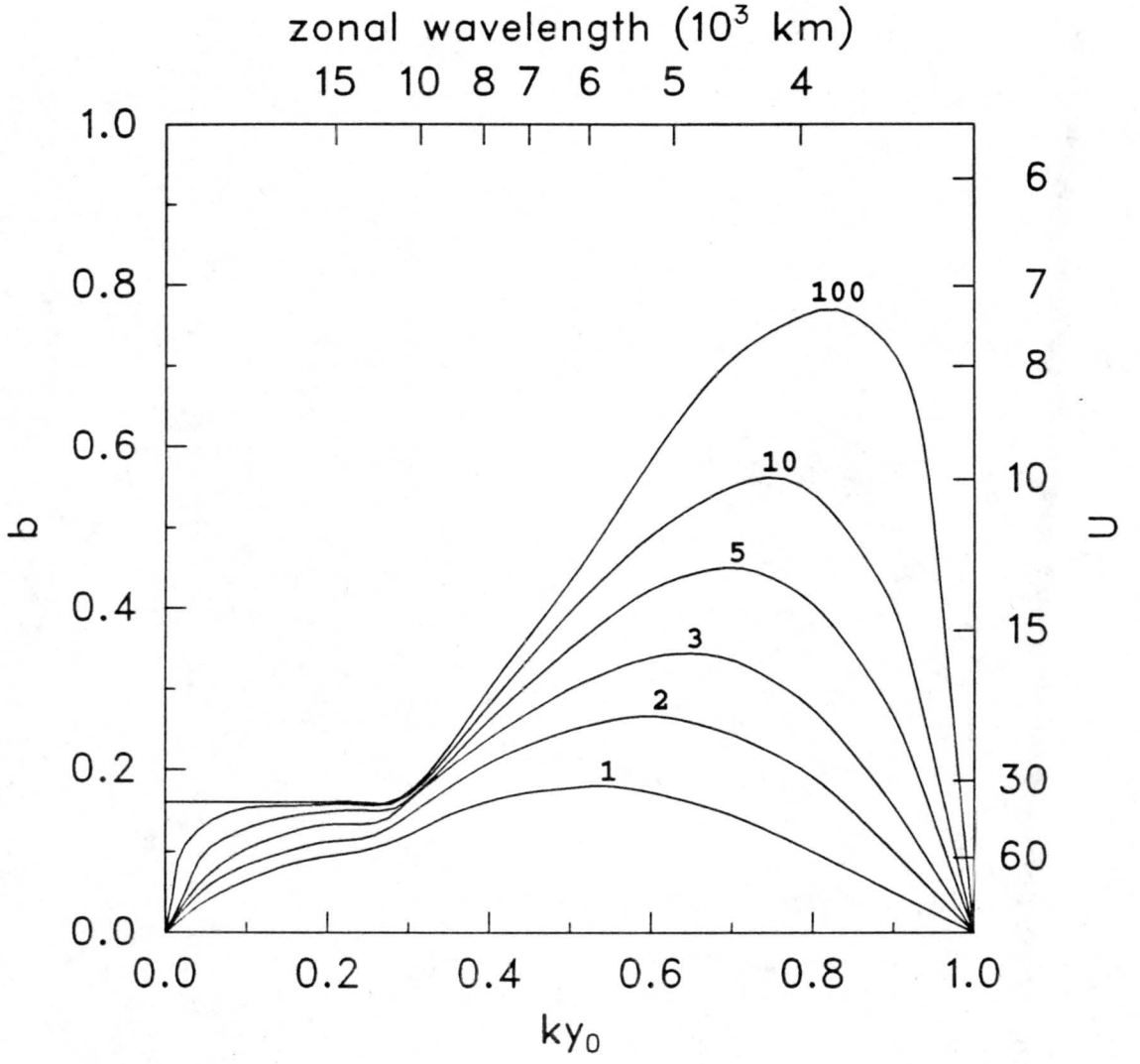

Figure 7. Reinterpretation of Kuo's (1973) growth rate diagram for the hyperbolic tangent shear layer. Isolines represent dimensionless growth rate $kc_i/(\beta y_0)$ as a function of $b = \beta y_0^2/U$ and the dimensionless wavenumber ky_0. To aid in physical interpretation we have labeled the isolines in terms of the e-folding time in days, the ordinate in terms of U (ms^{-1} on the right) and the abscissa in terms of zonal wavelength (km on the top), all for the choices $\beta = 2.235 \times 10^{-11}$ $\mathrm{m}^{-1}\mathrm{s}^{-1}$ and $y_0 = 500$ km.

increases from zero at $b \approx 0.77$ to a maximum at $b = 0$ and that the most unstable wavelength increases as the shear increases (b decreases), which is also the case for the Bickley jet. Most of the physics contained in the shear layer model can be more simply illustrated in the three region model described in the next subsection.

In passing we note that the hyperbolic tangent shear layer is also relevant to the understanding of westward moving undulations in the sea-surface temperature front which occurs near 3 N between the warm, eastward moving north equatorial countercurrent and the cold, westward moving south equatorial current. Observational analysis of this phenomenon has been made by Legeckis and his collaborators (1977, 1983, 1986) while a barotropic instability analysis has been given by Philander (1978, 1990).

d. three region model

Following the classical approach described by Rayleigh (1945, pages 392–394), Gill (1982, section 13.6), Haurwitz (1949) and Lipps (1970), let us consider a three region model in which the basic state zonal flow has the form

$$\bar{u}(y) = \begin{cases} U + \frac{\beta}{2}(y - y_0)^2 & y_0 \le y < \infty \\ Uy/y_0 + \frac{\beta}{2}(y^2 - y_0^2) & -y_0 \le y \le y_0 \\ -U + \frac{\beta}{2}(y + y_0)^2 & -\infty < y \le -y_0 \end{cases} \tag{4.23}$$

where U and y_0 are specified constants. This is essentially a shear layer flow with $\bar{u} = U$ at $y = y_0$ and $\bar{u} = -U$ at $y = -y_0$. By differentiation of (4.23) we can easily obtain

$$\bar{\zeta}(y) = f_0 + \beta y - \frac{d\bar{u}}{dy} = \begin{cases} f_0 + \beta y_0 & y_0 < y < \infty \\ f_0 - U/y_0 & -y_0 < y < y_0 \\ f_0 - \beta y_0 & -\infty < y < -y_0 \end{cases} \tag{4.24}$$

so that the basic state absolute vorticity $\bar{\zeta}$ is piecewise constant, as shown by the dotted line in Fig. 6. The central region ($-y_0 \le y \le y_0$) represents an ITCZ which lies south of the equator. Large negative absolute vorticity occurs in the ITCZ region. At $y = y_0$ there is a concentrated positive gradient of absolute vorticity while at $y = -y_0$ there is a concentrated reversed gradient of absolute vorticity.

Except along the lines $y = \pm y_0$, $\bar{\zeta}_y = \beta - \bar{u}_{yy} = 0$ so from (4.21) we conclude that $d^2\Psi/\partial y^2 - k^2\Psi = 0$. Thus, nonzero perturbation vorticity occurs only along $y = \pm y_0$, with the perturbation flow being irrotational elsewhere. As solutions of (4.20) which are bounded as $|y| \to \infty$, we have

$$\psi(x, y, t) = \left(\Psi_s e^{-k|y+y_0|} + \Psi_n e^{-k|y-y_0|}\right) e^{ik(x-ct)}, \tag{4.25}$$

where Ψ_s and Ψ_n are constants. Note from (4.25) that ψ and hence $v' = \partial\psi/\partial x$ are continuous at $y = \pm y_0$. The solution associated with the constant Ψ_s has vorticity anomalies concentrated at $y = -y_0$, so that the corresponding solution for ψ decays away in both directions from $y = -y_0$. Similarly, the solution associated with the constant Ψ_n has vorticity anomalies concentrated at $y = y_0$ and the corresponding solution for ψ decays away from $y = y_0$. Integrating (4.21) over a narrow region centered on either $y = -y_0$ or $y = y_0$, we obtain

$$(\bar{u} - c)\Delta\left(\frac{d\Psi}{dy}\right) + \Psi\Delta\bar{\zeta} = 0 \quad \text{at} \quad y = \pm y_0, \tag{4.26}$$

where Δ stands for the jump across the narrow region. Substituting (4.25) into (4.26) we obtain

$$-c_n e^{-2ky_0}\Psi_s + (c - U - c_n)\Psi_n = 0 \qquad (y = y_0), \tag{4.27}$$

$$(c + U - c_s)\Psi_s - c_s e^{-2ky_0}\Psi_n = 0 \qquad (y = -y_0), \tag{4.28}$$

where

$$c_n = -\frac{U(b+1)}{2ky_0}, \qquad c_s = -\frac{U(b-1)}{2ky_0}, \qquad b = \frac{\beta y_0^2}{U}.$$

If the basic state vorticity jump at the southern interface were removed, the first term in (4.27) would disappear and the Rossby wave on the northern interface would propagate with phase speed $c = U + c_n$. Similarly, if the basic state vorticity jump at the northern interface were removed, the second term in (4.28) would disappear and the Rossby wave on the southern interface would propagate with phase speed $c = -U + c_s$. For a typical active monsoon situation, $U > 0$ and $0 < b < 1$ so that $c_n < 0$ and $c_s > 0$, i.e., the noninteracting Rossby wave on the northern interface propagates westward relative to the eastward zonal flow on the normal poleward gradient of basic state vorticity, while the noninteracting Rossby wave on the southern interface propagates eastward relative to the westward zonal flow on the reversed poleward gradient of basic state vorticity. Thus, the system (4.27)–(4.28) can be regarded as a concise mathematical description of the interaction of two counterpropagating Rossby waves. The first term in (4.27) gives the effect of the southern vorticity anomaly pattern on the behavior of the northern interface, while the second term in (4.28) gives the effect of the northern vorticity anomaly pattern on the behavior of the southern interface. Note that the effect of these interactions decays with increasing wavenumber and increasing shear layer width according to e^{-2ky_0}.

Regarding (4.27) and (4.28) as a linear homogeneous system in the unknowns Ψ_s and Ψ_n, we require that the determinant of the coefficients vanish, which yields the eigenvalue relation

$$\frac{ky_0c}{U} = -\tfrac{1}{2}b \pm \left[\left(\tfrac{1}{2} - ky_0\right)^2 + \tfrac{1}{4}(b^2-1)e^{-4ky_0}\right]^{\frac{1}{2}}. \tag{4.29}$$

Thus, if we calculate the complex eigenvalue c from (4.29), use this result in (4.27) or (4.28) to determine the ratio between Ψ_s and Ψ_n, and then use this ratio in (4.25), we will have determined the corresponding eigenfunction ψ to within a multiplicative constant. From (4.29) we note that $|b| < 1$ is a necessary condition for instability. For unstable flows the dimensionless phase speed and growth rate are

$$\frac{c_r}{U} = -\frac{b}{2ky_0}, \qquad \frac{kc_i}{\beta y_0} = \frac{1}{b}\left[\tfrac{1}{4}(1-b^2)e^{-4ky_0} - \left(\tfrac{1}{2} - ky_0\right)^2\right]^{\frac{1}{2}}. \tag{4.30}$$

Note that $c_r = \frac{1}{2}(c_n + c_s)$, i.e., the phase speed of the barotropically unstable disturbance is simply the average speed of the noninteracting Rossby waves on the two interfaces.

Isolines of the dimensionless phase speed c_r/U and growth rate $kc_i/(\beta y_0)$ as functions of ky_0 and b are displayed for $y_0 = 500$ km and 300 km in Figs. 8a and 8b, respectively. As indicated by the star symbol in Fig. 8a, the model parameters which best describe the lower tropospheric zonal flow over AMEX during the active period in Fig. 2 are $U = 12$ ms^{-1} and $y_0 = 500$ km. The arrows in Fig. 8a depict how the wind shear across the monsoon trough increases with time for the two runs of the zonally symmetric model described in section 3. For example, after 60 hours of ITCZ convection the low level wind shear across an ITCZ at 15 S is approximately 10 ms^{-1}/500 km. At this value of shear, the three region model predicts the presence of barotropic instability with an e-folding time of approximately three days. Furthermore, these arrows suggest that ITCZ's become barotropically unstable sooner as their latitudinal position shifts poleward. Comparison of Fig. 8a with 8b shows that the most unstable wavelength is a function of the width of the shear region such that as y_0 decreases the most unstable wavelengths become shorter. As in Kuo's results (Fig. 7), the three region model (Fig. 8) shows that the most unstable wavelength increases as b is decreased. Although Figs. 7 and 8 are similar, there are differences for very long waves (small ky_0). This is due to the lack of a background absolute vorticity gradient in the three region model (compare the solid and dotted curves in the middle panel of Fig. 6).

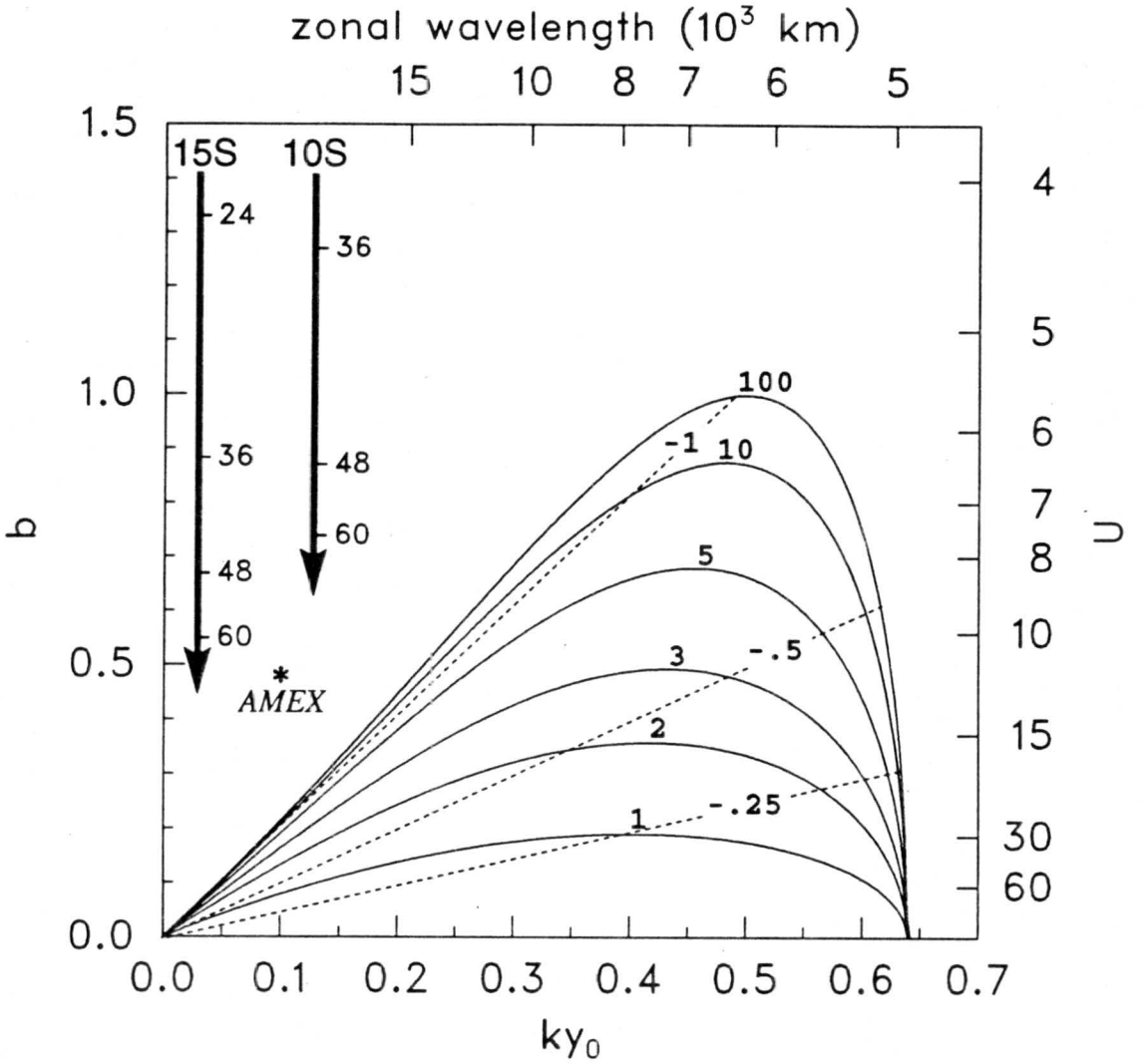

Figure 8a. Isolines of the dimensionless phase speed c_r/U (dashed) and growth rate $kc_i/(\beta y_0)$ (solid) as a function of $b = \beta y_0^2/U$ and the dimensionless wavenumber ky_0 for the three region model. To aid in physical interpretation we have labeled the isolines of growth rate in terms of the e-folding time in days, the ordinate in terms of U (ms^{-1} on the right) and the abscissa in terms of zonal wavelength (km on the top), all for the choices $\beta = 2.235 \times 10^{-11}$ $m^{-1}s^{-1}$ and $y_0 = 500$ km. The arrows depict how the wind shear across the monsoon trough increases with time for an ITCZ centered at 15 S and 10 S. The numbers plotted along these arrows denote the time (hours) at which the Hadley cell model developed a given wind shear. The star labeled AMEX represents the observed value of wind shear across the monsoon trough during a period of intense convection (taken from Fig. 2).

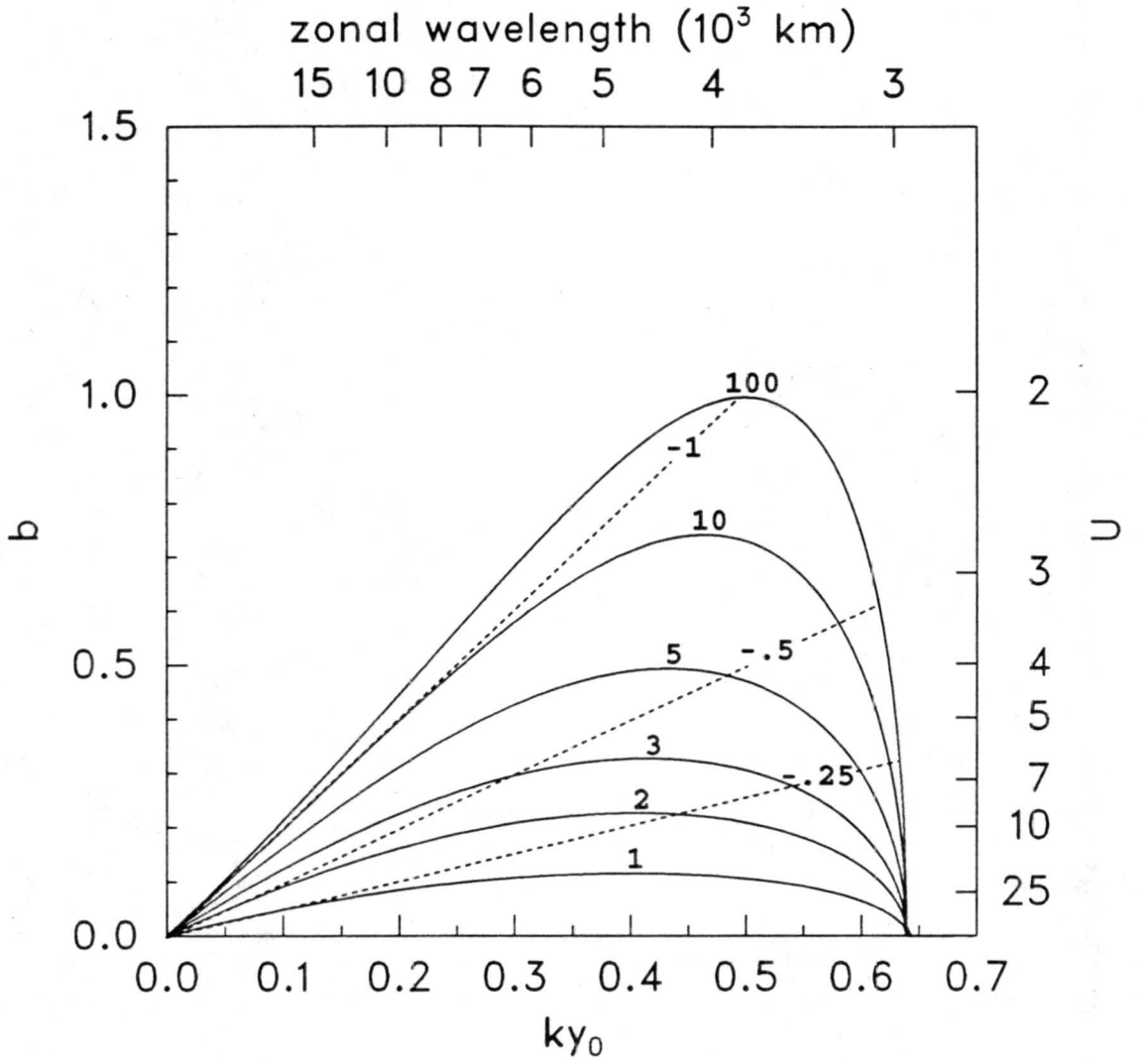

Fig. 8b. Same as Fig. 8a, except $y_0 = 300$ km.

Turning our attention to the eigenfunction, we now note that the first part of (4.25) represents the streamfunction pattern associated with the chain of vorticity anomalies along the line $y = -y_0$, while the second part represents the pattern associated with the anomalies along the line $y = y_0$. In Fig. 9a we have plotted the total streamfunction solution determined from (4.25) for the most unstable wave when $b = 0.46$. The part of the total solution associated with the constant Ψ_n is shown in Fig. 9b, and that associated with the constant Ψ_s in Fig. 9c. By superimposing Figs. 9b and 9c we can see the mutual influence of the two chains of vorticity anomalies. To aid in understanding this mutual influence we have constructed the schematic shown in Fig. 10. The amplitude of the undulations in this figure are proportional to the meridional particle displacements which, in turn, are proportional to the voriticty jumps ($\Delta\bar{\zeta}$) at the interfaces (cf. dotted line in middle panel of Fig. 6). The other values shown in Fig. 10 were computed from (4.28) and (4.29) using the same model parameters as those for Figs. 8a and 9.

The mechanism of monsoon shear zone breakdown for the most unstable normal mode can now be summarized as follows (see Fig. 10). The original undisturbed state consists of a strip of negative vorticity, with westerlies to the north and easterlies to the south. Fluid displaced away from the central strip leads to negative vorticity anomalies while fluid displaced toward the strip leads to positive vorticity anomalies, as indicated by the open sign symbols on the northern interface and the solid sign symbols on the southern interface. The open arrows represent the flow induced by the northern chain of vorticity anomalies, while the solid arrows give the flow induced by the southern chain. At the points along the wavy northern interface where there is no interface displacement, the northern vorticity anomalies induce a displacement which tends to propagate the northern wave westward ($c_n = -21.6$ ms^{-1}), but the southern vorticity anomalies induce a displacement which tends to propagate the northern wave eastward at 2.8 ms^{-1}. Similarly, at the points along the wavy southern interface where there is no interface displacement, the southern vorticity anomalies induce a displacement which tends to propagate the southern wave eastward ($c_s = 8$ ms^{-1}), but the northern vorticity anomalies induce a displacement which tends to propagate the southern wave westward at 2.8 ms^{-1}. With the basic zonal flow included, the net result is that the waves are phase locked and propagate westward ($c_r = -6.8\text{ms}^{-1}$). In addition, displaced fluid particles on the northern interface will be even further displaced by the flow induced by the vorticity anomalies of the southern interface, and vice versa. This interdependence between the two counterpropagating Rossby waves has been eloquently described by Hoskins

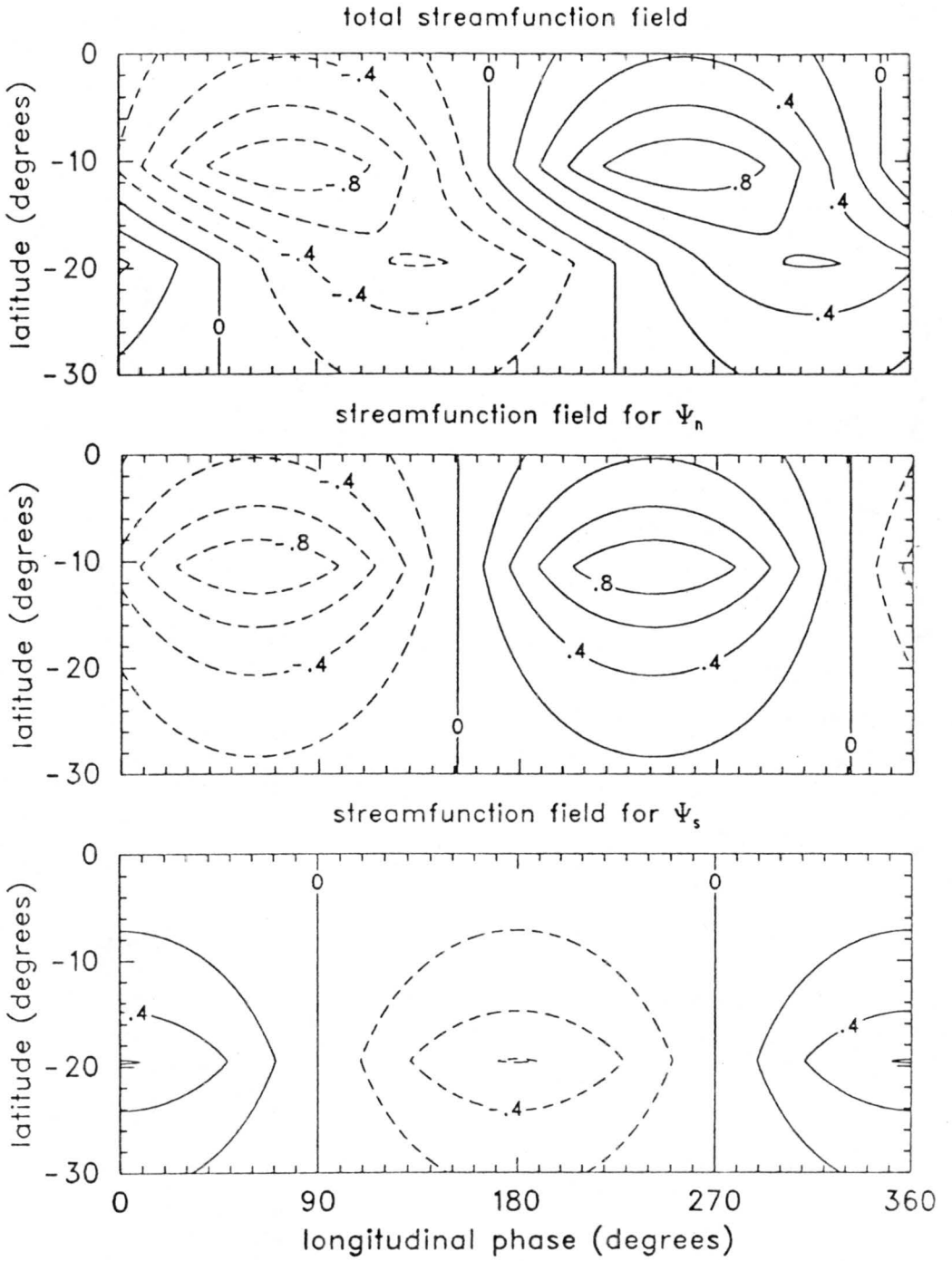

Figure 9. Top panel shows the total streamfunction solution determined from (4.25). The part of the total solution associated with the constant Ψ_n is shown in the middle panel, and that associated with the constant Ψ_s in the bottom panel. These fields have been normalized by the maximum streamfunction value.

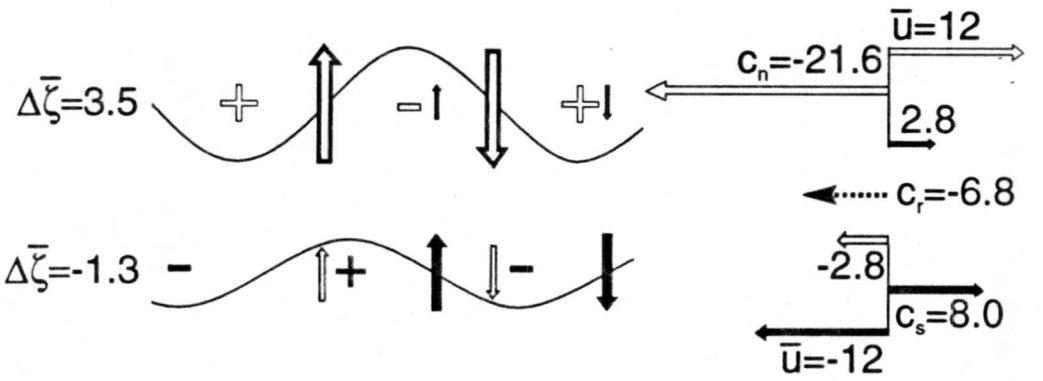

Figure 10. Interpretation of monsoon trough shear zone breakdown through barotropic instability. The moist convection of the monsoon trough produces a zonal strip of enhanced negative vorticity, with associated positive and negative jumps of vorticity at the northern and southern interfaces of the strip with the surrounding fluid (units are 10^{-5} s^{-1}). Undulations on the interfaces produce chains of vorticity anomalies indicated by the open (northern) and solid (southern) sign symbols. The Rossby restoring mechanism tends to propagate the northern chain to the west ($c_n = -21.6$ ms^{-1}) and the southern chain to the east ($c_s = 8$ ms^{-1}). The mutual influence of the two chains is to slow these two propagation speeds by 2.8 ms^{-1}, which (along with the effects of $\bar{u}$) results in phase locking and westward propagation of the whole pattern ($c_r = -6.8$ ms^{-1}). In addition the southern chain of vorticity anomalies induces a flow (solid arrows on northern interface) which amplifies the displacements of the northern chain, and vice versa. In this way there is both phase locking and growth.

et al. (1985, section 6b) as follows: "The induced velocity field of each Rossby wave keeps the other in step, and makes the other grow."

e. nonlinear regime

There are many interesting nonlinear aspects to the barotropic instability problem. Elegantly illustrated discussions of the nonlinear regime can be found in a paper by Lesieur et al. (1988) and in the recent textbook by Lesieur (1990, section 3.1 and Plates 7–8), who has described the time evolution of an unstable hyperbolic tangent shear layer in terms of the formation of fundamental eddies and the successive pairing or merging of these eddies.

Further insight into the nonlinear evolution of unstable waves in a shear layer has been obtained by Dritschel (1989), Pratt et al. (1991) and Pratt and Pedlosky (1991) using the method of contour dynamics (Zabusky et al. 1979, Zabusky and Overman 1983, Dritschel 1988). The method is specifically designed for piecewise-constant vorticity distributions such as the one used in our three region model. Basically, one simply predicts the position of the contours separating the regions of constant vorticity. An initial unstable strip of uniform vorticity with small undulations on its northern and southern contours can distort and evolve into a pattern in which the vorticity becomes "pooled" into rotating elliptical regions connected to each other by filaments or strands of high vorticity fluid. For the Australian monsoon case this nonlinear evolution is schematically illustrated in Fig. 11. The pattern is reminiscent of satellite images showing pooled and filamented regions of cumulus convection during ITCZ breakdown (see Hack et al. 1989, Fig. 1 for an Eastern Pacific example). At later times the pooled regions become more symmetric and the filaments thinner. This demonstrates the remarkable fact that the fundamental (and nonlinear) dynamics necessary to transform an ITCZ zonal strip of potential vorticity into nearly axisymmetric tropical cyclones is inherent in a simple three region nondivergent barotropic model.

In concluding this section we would like to make two additional comments. First, by using the preceeding barotropic analysis we do not wish to imply that the breakdown of the ITCZ is a purely barotropic process. Certainly, baroclinic and moist physical processes must play an important role. However, there does appear to be a strong underlying component which is fundamentally barotropic in nature. Second, we note that the counterpropagating Rossby wave interpretation of barotropic instability is not the only way we can understand the breakdown of the ITCZ. Another interpretation of barotropic instability is provided by an argument

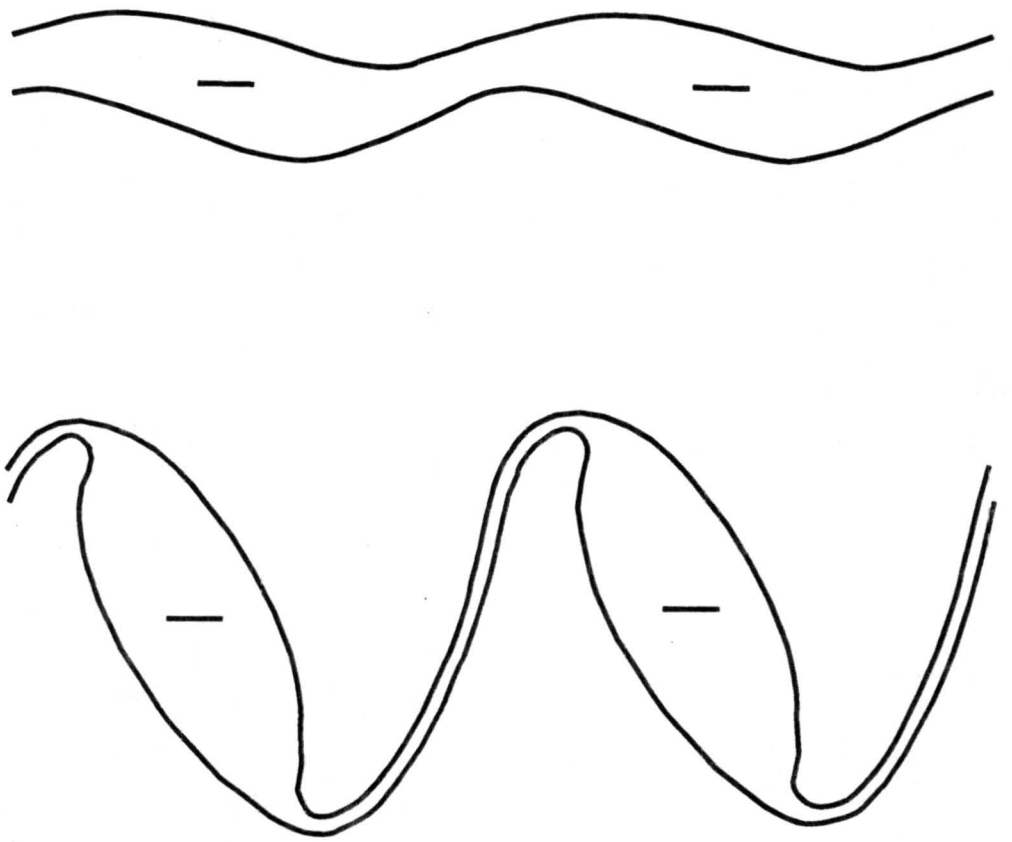

Figure 11. Schematic illustration of the nonlinear development of a zonal strip of enhanced negative vorticity. The most unstable configuration (upper diagram) grows nonlinearly into elliptical regions of pooled vorticity connected by thin filaments. At later times the pooled regions become more symmetrical.

based on wave overreflection from critical latitudes (see Lindzen and Tung 1978, McIntyre and Weissman 1978, and the review article of Lindzen 1988). According to this argument the Rayleigh and Fjørtoft necessary conditions for barotropic instability are also sufficient conditions for the existence of overreflected waves. The conditions are that $d\bar{\zeta}/d\phi$ change sign in the domain, that a critical latitude exist (in the hyperbolic tangent shear layer case of Fig. 6 the critical latitude lies within the region of $d\bar{\zeta}/d\phi < 0$), and that Rossby waves are overreflected at the critical latitude and contained in such a way as to be repeatedly overreflected. Although considerable progress toward understanding barotropic and baroclinic instability can be made using the concepts of wave overreflection, the method is more mathematically involved and perhaps (to most) less intuitive than the counterpropagating Rossby wave arguments given above.

5. Divergent barotropic instability of the monsoon trough shear zone

Some of the nondivergent barotropic stability theorems of the previous section can be generalized to the divergent barotropic model and to discretely layered (but not continuously stratified) primitive equation models on the β-plane and sphere (Ripa 1983, 1991). For the spherical shallow water case we consider the linearized equations

$$\frac{\partial u'}{\partial t} + \bar{u}\frac{\partial u'}{a\cos\phi\partial\lambda} + v'\frac{\partial \bar{u}}{a\partial\phi} - \left(2\Omega\sin\phi + \frac{\bar{u}\tan\phi}{a}\right)v' + g\frac{\partial h'}{a\cos\phi\partial\lambda} = 0, \tag{5.1}$$

$$\frac{\partial v'}{\partial t} + \bar{u}\frac{\partial v'}{a\cos\phi\partial\lambda} + \left(2\Omega\sin\phi + \frac{2\bar{u}\tan\phi}{a}\right)u' + g\frac{\partial h'}{a\partial\phi} = 0, \tag{5.2}$$

$$\frac{\partial h'}{\partial t} + \bar{u}\frac{\partial h'}{a\cos\phi\partial\lambda} + v'\frac{\partial \bar{h}}{a\partial\phi} + \bar{h}\left(\frac{\partial u'}{a\cos\phi\partial\lambda} + \frac{\partial(v'\cos\phi)}{a\cos\phi\partial\phi}\right) = 0, \tag{5.3}$$

where the primes denote small perturbations about a purely zonal basic flow, $\bar{u}(\phi)$, with associated depth $\bar{h}(\phi)$.

To derive Ripa's theorem we need to combine (5.1)–(5.3) into equations for

$$E' = \tfrac{1}{2}\left[\bar{h}(u'^2 + v'^2) + 2\bar{u}u'h' + gh'^2\right], \tag{5.4}$$

$$M' = h'u'a\cos\phi, \tag{5.5}$$

and

$$P' = \frac{1}{\bar{h}}\left(\frac{\partial v'}{a\cos\phi\partial\lambda} - \frac{\partial(u'\cos\phi)}{a\cos\phi\partial\phi} - \bar{P}h'\right), \tag{5.6}$$

where $\bar{P} = [2\Omega \sin\phi - \partial(\bar{u}\cos\phi)/a\cos\phi\partial\phi]/\bar{h}$. To derive the equation for E' we form $(\bar{h}u' + h'\bar{u}) \cdot (5.1) + (\bar{h}v') \cdot (5.2) + (\bar{u}u' + gh') \cdot (5.3)$ to obtain

$$\frac{\partial E'}{\partial t} + \bar{h}^2 \bar{u} v' P' + \frac{\partial[(\bar{u}u' + gh')(\bar{h}u' + h'\bar{u})]}{a\cos\phi\partial\lambda} + \frac{\partial[(\bar{u}u' + gh')\bar{h}v'\cos\phi]}{a\cos\phi\partial\phi} = 0. \quad (5.7)$$

Integrating (5.7) over the surface of the earth we obtain

$$\iint \left(\frac{\partial E'}{\partial t} + \bar{h}^2 v' P' \bar{\omega} a \cos\phi \right) \cos\phi \, d\lambda \, d\phi = 0, \quad (5.8)$$

where the basic state angular velocity $\bar{\omega}$ is related to the basic state zonal wind $\bar{u}$ by $\bar{u} = \bar{\omega} a \cos\phi$. To derive the equation for M' we form $(h' a\cos\phi) \cdot (5.1) + (u' a \cos\phi) \cdot (5.3)$. Integrating the result over the surface of the earth we obtain

$$\iint \left(\frac{\partial M'}{\partial t} + \bar{h}^2 v' P' a \cos\phi \right) \cos\phi \, d\lambda \, d\phi = 0. \quad (5.9)$$

Multiplying (5.9) by the constant ω_0, and then subtracting the result from (5.8), we obtain

$$\iint \left(\frac{\partial (E' - \omega_0 M')}{\partial t} + \bar{h}^2 v' P' (\bar{\omega} - \omega_0) a \cos\phi \right) \cos\phi \, d\lambda \, d\phi = 0. \quad (5.10)$$

The equation for P', obtained by forming the vorticity equation from (5.1)–(5.2) and then eliminating the divergence using (5.3), takes the form

$$\frac{\mathcal{D}P'}{\mathcal{D}t} + \frac{d\bar{P}}{a d\phi} v' = 0, \quad (5.11)$$

where $\mathcal{D}/\mathcal{D}t$ is the same operator used in (4.5a). Again, defining the meridional particle displacement η by $\mathcal{D}\eta/\mathcal{D}t = v'$, we can integrate (5.11) to obtain

$$P' + \frac{d\bar{P}}{a d\phi} \eta = 0, \quad (5.12)$$

which is a generalization of (4.4). Multiplication of (5.12) by v' yields

$$v'P' + \frac{\mathcal{D}}{\mathcal{D}t} \left(\frac{d\bar{P}}{a\, d\phi} \tfrac{1}{2} \eta^2 \right) = 0. \quad (5.13)$$

Finally, using (5.13) in (5.10) for $v'P'$ we obtain

$$\frac{d}{dt} \iint \left(E' - \omega_0 M' + \bar{h}^2 \frac{\partial \bar{P}}{a\partial\phi} \tfrac{1}{2} \eta^2 (\omega_0 - \bar{\omega}) a \cos\phi \right) \cos\phi \, d\lambda \, d\phi = 0, \quad (5.14)$$

which is the divergent barotropic generalization of the nondivergent barotropic result (4.7). We now argue that, if $E' - \omega_0 M' \geq 0$ and $(\omega_0 - \bar{\omega})\partial\bar{P}/\partial\phi \geq 0$, the constraint (5.14) does not allow η^2 to grow in an overall sense. From (5.4) we note that $E' \geq 0$ if $\bar{u}^2 \leq g\bar{h}$. By a similar argument, $E' - \omega_0 M' \geq 0$ if $[(\omega_0 - \bar{\omega})a\cos\phi]^2 \leq g\bar{h}$. We can now state Ripa's shallow water generalization of the theorems of Rayleigh and Fjørtoft. *If there exists any value of* ω_0 *such that*

$$(\omega_0 - \bar{\omega})\frac{\partial\bar{P}}{\partial\phi} \geq 0 \qquad \text{and} \qquad [(\omega_0 - \bar{\omega})a\cos\phi]^2 \leq g\bar{h} \tag{5.15a, b}$$

for all ϕ*, then the flow is stable to infinitesimal perturbations.* Ripa has also discussed several corollaries of (5.15), one of which is obtained by choosing $\omega_0 = \max[\bar{\omega}]$. This results in the following weaker sufficient condition for stability. *If*

$$\frac{\partial\bar{P}}{\partial\phi} \geq 0 \qquad \text{and} \qquad \max[\bar{\omega}] \leq \min\left[\bar{\omega} + \frac{(g\bar{h})^{1/2}}{a\cos\phi}\right] \tag{5.16a, b}$$

for all ϕ*, then the flow is stable to infinitesimal perturbations.*

To recover the stability results for the nondivergent barotropic model from the stability results for the divergent barotropic model we consider the limit $g\bar{h} \to \infty$, in which case (5.15b) is satisfied for any finite ω_0. Then, there is no difference between vorticity and potential vorticity, and a choice of ω_0 such that $\omega_0 - \bar{\omega}(\phi) < 0$ everywhere leads to $d\bar{\zeta}/d\phi \leq 0$ everywhere as sufficient for stability, while a choice of ω_0 such that $\omega_0 - \bar{\omega}(\phi) > 0$ everywhere leads to $d\bar{\zeta}/d\phi \geq 0$ everywhere as sufficient for stability. Thus, a necessary condition for instability is that $d\bar{\zeta}/d\phi$ have both signs (Rayleigh's theorem). It is also of interest to note that, if $d\bar{\zeta}/d\phi = 0$ at $\phi = \hat{\phi}$, then the choice $\omega_0 = \bar{\omega}(\hat{\phi})$ leads from (5.15a) to $[\bar{\omega}(\hat{\phi}) - \bar{\omega}(\phi)]d\bar{\zeta}/d\phi < 0$ somewhere as a necessary condition for instability (Fjørtoft's theorem).

In applications of shallow water stability theory to atmospheric data or to the interpretation of atmospheric models with continuous stratification there is considerable freedom in the choice of mean depth. However, reasonable $\bar{h}$'s should probably exceed 100m. For such $\bar{h}$'s, the zonal flows generated by a few days of ITCZ convection satisfy neither (5.16) nor the more general condition (5.15). Again, to actually confirm that the monsoon zonal flow is unstable in the divergent barotropic model, an eigenvalue-eigenfunction calculation is useful. Thus, let us now use the linearized shallow water equations (5.1)–(5.3) as the basis for a calculation of the growth rates and associated structures for wave disturbances on the observed zonally averaged basic state. The present discussion is meant to complement Dunkerton's (1990)

recent detailed investigation of the effects of horizontal divergence on barotropic instability. The solution method for the present model is described in detail in Stevens and Ciesielski (1986). For a given zonal wavenumber, fluid depth $\bar{h}$ and basic state zonal flow $\bar{u}$, the model computes a set of complex eigenvalues $(\sigma_r + i\sigma_i)$ and corresponding eigenfunctions (u', v', gh'). A positive imaginary part indicates an unstable mode where σ_i is the growth rate. The real part of the eigenvalue is related to the zonal phase speed such that $\sigma_r > 0$ implies an eastward propagating phase speed.

For our present model calculations, the basic state used was taken from the sector average winds in Fig. 2 at 315 K (700 mb) which is the level of the lower tropospheric zonal wind maxima. This wind profile and associated vorticity distribution are shown in Fig. 13. In the shallow water model, potential and absolute vorticity are related by $P = \zeta/h$. For the present model the necessary condition for inertial instability to occur is that $f\bar{P} < 0$ (Stevens 1983), whereas for barotropic instability the necessary condition is that $\partial\bar{P}/\partial\phi < 0$ somewhere in the fluid (Ripa 1983). Both of these conditions are met in the $\bar{P}$ profile implied by Fig. 13. For this basic state $\bar{u}$ field, the computed growth rates (σ_i) are shown as a function of zonal wavenumber in Fig. 12 for several values of equivalent depth. As seen here, two distinct types of instabilities are present, the characteristics of which are described below.

Inertial instability results in two of the modes (depicted with dashed lines) in Fig. 12. The first of these with an e-folding time less than 2 days occurs at the smallest equivalent depth ($h = 0.01$m) examined here. This inertial instability mode with maximum growth rate on the symmetric axis is commonly referred to as symmetric instability. Despite its fast growth rate, Dunkerton (1981) has pointed out that a scale-selective dissipation process will act to stabilize instabilities at these short vertical scales. As the vertical scale increases, the growth rates of the inertial instability mode decrease rapidly. For example at $\bar{h} = 1$m, the e-folding time for inertial instability is greater than 5 days. This mode is centered near 2 S (i.e., in the region where $f\bar{P} < 0$) and is confined latitudinally to within 5 degrees of this latitude. With its slow growth rate it is uncertain how much this mode would amplify against the atmosphere's dissipative effects to be an effective mechanism for restoring the atmosphere to a state where $f\bar{P} > 0$. The phase speed for these modes is nearly independent of zonal wavenumber and is ~ 6 ms^{-1}.

Barotropic instability results in the other two modes (depicted with solid lines) in Fig. 12. The e-folding time for these modes attains a minimum of 2.7 days (for

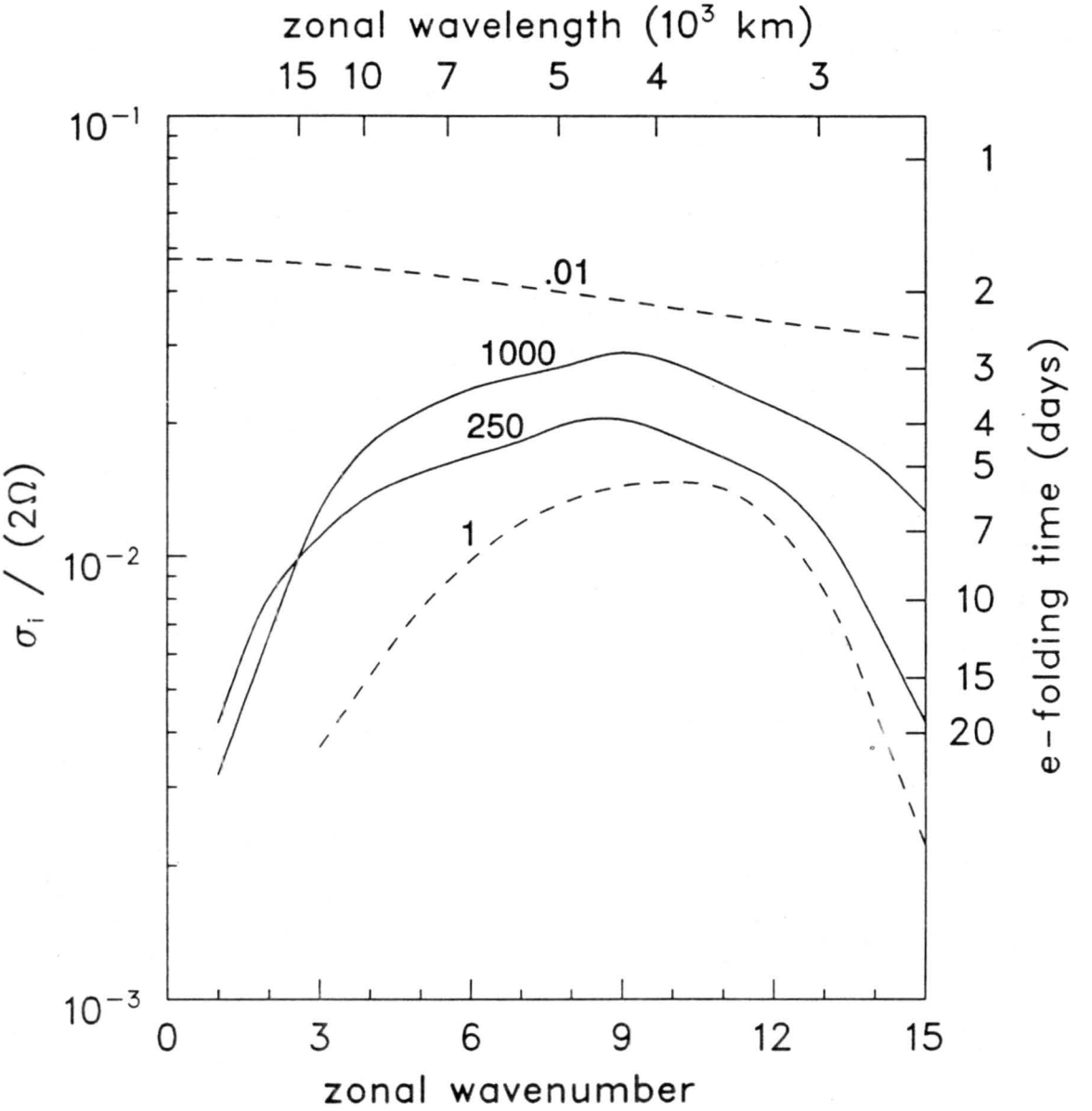

Figure 12. Nondimensional growth rates associated with the zonal wind profile in the middle panel of Fig. 13 as a function of zonal wavenumber (bottom scale) or zonal wavelength (top scale). Values along the curves represent the equivalent depth in meters. Scale on the right gives the e-folding time in days. The dashed lines represent inertial instabilities and the solid lines barotropic instabilities.

$\bar{h}$ = 1000m) and 3.9 days (for $\bar{h}$ = 250m). This effect of decreasing growth rate with decreasing equivalent depth (or increasing divergence) is consistent with Philander's (1976) analysis, which shows that divergence stablilizes barotropic instabilities associated with shear layers. The corresponding period and phase speed for both barotropic modes in Fig. 12 is approximately 7.7 days and -6.3 ms^{-1}, respectively. These growth rates and phase speeds compare quite favorably with those obtained from the three-region model, with the exception that the wavelength of maximum instability for the present model (4200 km) is considerably shorter than that found by the three-region model for y_0 = 500 km (7000 km, cf. Fig. 8a).

The eigenfunction corresponding to the most unstable barotropic mode is shown in Fig. 13 for the $\bar{h}$=250m case. The maxima in the perturbation geopotential and winds are centered near 20 S which is in the region of the reversed PV gradient. Equatorward of this latitude the perturbations fields exhibit a southeast-northwest slope. This tilt of the disturbance axis is in the opposite direction to the shear profile (middle panel of Fig. 13) and is characteristic of a barotropically unstable wave in which $\overline{u'v'}$ has the opposite sign to $d\bar{u}/d\phi$ (Haltiner and Williams 1980). It is interesting to note the similarity between the modal structure in Fig. 13 and the observed instantaneous perturbation winds during an active period over the AMEX region (Fig. 14). In this figure one can detect a wave-like feature with a maximum perturbation near 20 S, a southeast-northwest tilt and a wavelength of ~4500 km. These general characteristics were observed at several times during active phases of AMEX. Despite the limitations of the model used here, specifically the lack of moist physics and vertical structure, the similarity between the observed and modeled fields suggests that barotropic instability plays an important role in the dynamics of the AMEX region.

6. Concluding remarks

Through the use of a zonally symmetric balanced model we have shown that the potential vorticity in the monsoon trough evolves in such a way as to produce a region of reversed poleward gradient of potential vorticity on the poleward side of the trough in the lower troposphere and on the equatorward side of the trough in the upper troposphere. This sets the stage for combined barotropic-baroclinic instability, with the barotropic process playing a crucial role.

We have studied the barotropic instability of the monsoon trough flows using both nondivergent and divergent barotropic models. For the nondivergent model

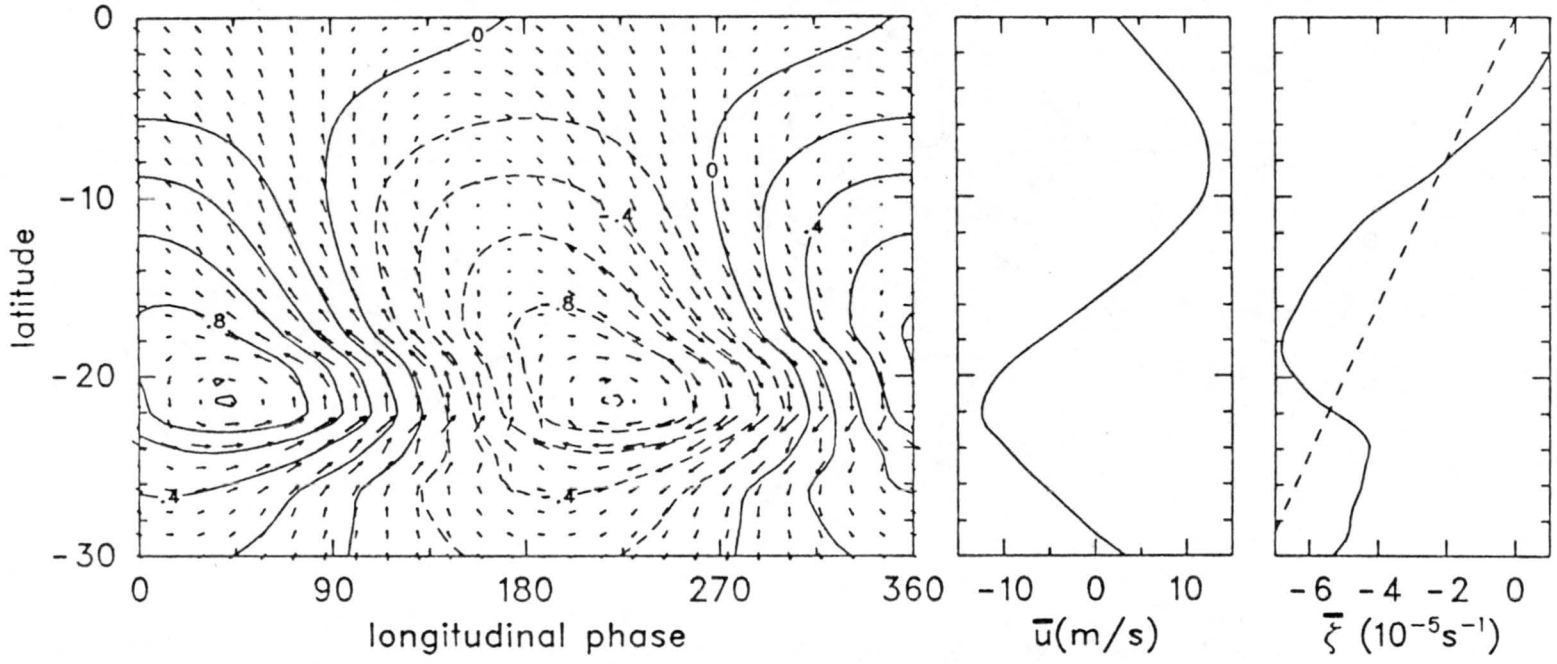

Figure 13. The left panel shows the eigenfunctions over one wavelength at maximum instability (zonal wavenumber 9) for $\bar{h} = 250$m and for the $\bar{u}$ profile in the middle panel, which comes from the sector average winds in Fig. 2 at 315 K. Arrows represent perturbation wind velocities and solid (dashed) lines show positive (negative) contours of perturbation geopotential. The geopotential field has been normalized by the maximum value of geopotential. The right panel shows the profile of $\bar{\zeta}$ (solid) associated with the $\bar{u}$ profile and f (dashed).

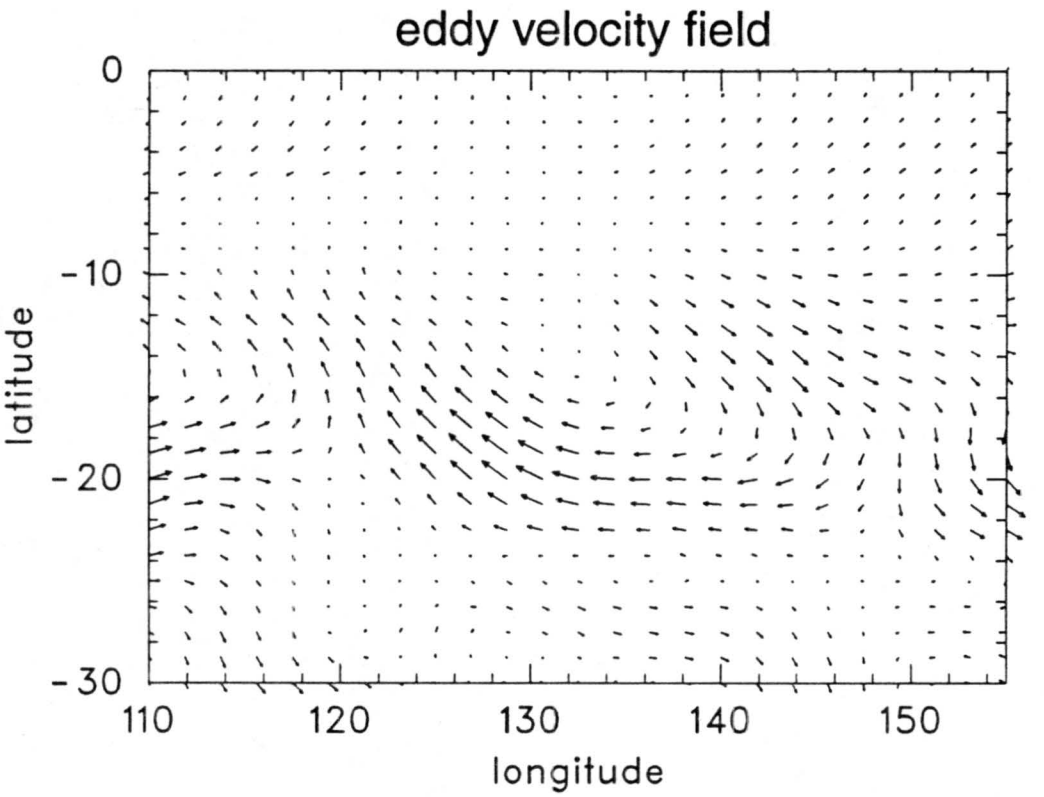

Figure 14. Instantaneous eddy velocity field at 700 mb for 1 February 1987 at 1100 UTC. These winds are deviations from the sector average (110–135 E) winds.

a useful idealization of the zonal flow produced by ITCZ convection is the hyperbolic tangent shear layer. For reasonable heating rates and widths, the hyperbolic shear layer can become sufficiently strong and narrow in 2–3 days so as to produce barotropically unstable waves with e-folding times of order 2 days. A further idealization of the hyperbolic tangent shear layer into a three region model leads to an explicit interpretation of the barotropically unstable modes in terms of phase locked counterpropagating Rossby waves. For the divergent barotropic model, a stability analysis of the zonal wind profile over the AMEX region has shown the existence of barotropic instability with the following characteristics: most unstable wavelength of 4200 km, e-folding time of 2.7 days, and phase speed of -6.3 ms^{-1}. The tilt of the disturbance axis (southeast–northwest) is opposite to the mean shear, which is characteristic of amplifying waves. Observations of a similar structure in the instantaneous AMEX velocity fields suggest that barotropic instability plays a major role in the evolution of wave disturbances over northern Australia.

These dynamical principles lead to the notion that many ITCZ regions of the world (e.g., northern Australia, northeast Pacific, northern Africa and the northeast Atlantic) share the same basic dynamics and are capable of in situ production of easterly waves through dynamic instability.

Acknowledgments We would like to thank Duane Stevens for making available his linear shallow water model, which was used in constructing Figs. 12 and 13. The present research was supported by the Office of Naval Research, under grant N000014-88-K-0214.

REFERENCES

Andrews, D. G., 1983: A conservation law for small-amplitude quasi-geostrophic disturbances on a zonally asymmetric basic flow. *J. Atmos. Sci.*, **40**, 85–90.

Arnol'd, V. I., 1965: Conditions for nonlinear stability of stationary plane curvilinear flows of an ideal fluid. *Dokl. Akad. Nauk. SSSR*, **162**, 975–978. (English tranlation: *Soviet Math.*, **6**, 773–777).

Arnol'd, V. I., 1966: On an a priori estimate in the theory of hydrodynamical instability. *Izv. Vyssh. Uchibn. Zaved. Matematika*, **54**, no. 5, 3–5. (English tranlation: *American Math. Soc. Transl., Series 2*, **79**, 267–269).

Burpee, R. W., 1972: The origin and structure of easterly waves in the lower troposphere of North Africa. *J. Atmos. Sci.*, **29**, 77–90.

Charney, J. G., and M. E. Stern, 1962: On the stability of internal baroclinic jets in a rotating atmosphere. *J. Atmos. Sci.*, **19**, 159–172.

Davidson, N. E., G. J. Holland, J. L. McBride and T. D. Keenan, 1990: On the formation of AMEX tropical cyclones Irma and Jason. *Mon. Wea. Rev.*, **118**, 1981–2000.

Dickinson, R., and F. J. Clare, 1973: Numerical study of the unstable modes of a hyperbolic-tangent barotropic shear flow. *J. Atmos. Sci.*, **30**, 1035–1049.

Drazin, P. G., and W. H. Reid, 1981: *Hydrodynamic Stability.* Cambridge Univ. Press, Cambridge, England.

Dritschel, D., 1988: Contour surgery: a topological reconnection scheme for extended integrations using contour dynamics. *J. Comput. Phys.*, **77**, 240–266.

Dritschel, D., 1989: On the stabilization of a two-dimensional vortex strip by adverse shear. *J. Fluid Mech.*, **206**, 193–221.

Dunkerton, T. J., 1981: On the inertial stability of the equatorial middle atmosphere. *J. Atmos. Sci.*, **38**, 2354–2365.

Dunkerton, T. J., 1990: Eigenfrequencies and horizontal structure of divergent barotropic instability originating in tropical latitudes. *J. Atmos. Sci.*, **47**, 1288–1301.

Eliassen, A., 1983: The Charney–Stern theorem on barotropic-baroclinic instability. *Pure Appl. Geophys.*, **121**, 563–572.

Frank, W. M., and J. L. McBride, 1989: The vertical distribution of heating in AMEX and GATE cloud clusters. *J. Atmos. Sci*, **46**, 3464–3478.

Gill, A. E., 1982: *Atmosphere-Ocean Dynamics.* Academic Press, 662 pages.

Gunn, B. W., J. L. McBride, G. J. Holland, T. D. Keenan, N. E. Davidson and H. H. Hendon, 1989: The Australian summer monsoon circulation during AMEX Phase II. *Mon. Wea. Rev.*, **117**, 2554–2574.

Hack, J. J., W. H. Schubert, D. E. Stevens and H.-C. Kuo, 1989: Response of the Hadley circulation to convective forcing in the ITCZ. *J. Atmos. Sci.*, **46**, 2957–2973.

Haltiner, G. J., and R. T. Williams, 1980: *Numerical Prediction and Dynamic Meteorology.* John Wiley and Sons, 477 pp.

Haurwitz, B., 1949: The instability of wind discontinuities and shear zones in planetary atmospheres. *J. Meteor.*, **6**, 200–206.

Haynes, P. H., 1988: Forced, dissipative generalizations of finite-amplitude wave-activity conservation relations for zonal and nonzonal basic flows. *J. Atmos. Sci.*, **45**, 2352–2362.

Hendon, H. H., N. E. Davidson, and B. Gunn, 1989: Australian summer monsoon onset during AMEX 1987. *Mon. Wea. Rev.*, **117**, 370–390.

Hendon, H. H., and B. Liebmann, 1990: A composite study of the onset of the Australian monsoon. *J. Atmos. Sci.*, **47**, 2227–2240.

Holland, G. J., 1986: Interannual variability of the Australian summer monsoon at Darwin: 1952–1982. *Mon. Wea. Rev.*, **114**, 594–604.

Hoskins, B. J., M. E. McIntyre and A. W. Robertson, 1985: On the use and significance of isentropic potential vorticity maps. *Quart. J. R. Met. Soc.*, **111**, 877–946.

Kuo, H.-L., 1973: Dynamics of quasigeostrophic flows and instability theory. *Adv. Appl. Mech.*, **13**, 247–330.

Legeckis, R., 1977: Long waves in the eastern equatorial Pacific: a view from a geostationary satellite. *Science*, **197**, 1179–1181.

Legeckis, R., 1986: A satellite time series of sea surface temperatures in the eastern equatorial Pacific Ocean, 1982–1986. *J. Geophys. Res.*, **91**, 12879–12886.

Legeckis, R., W. Pichel and G. Nesterczuk, 1983: Equatorial long waves in geostationary satellite observations and in a multichannel sea surface temperature analysis. *Bull. Amer. Meteor. Soc.*, **64**, 133–139.

Lesieur, M., 1990: *Turbulence in Fluids.* Kluwer Academic Publishers, 412 pages.

Lesieur, M., C. Staquet, P. LeRoy and P. Comte, 1988: The mixing layer and its coherence examined from the point of view of two-dimensional turbulence. *J. Fluid Mech.*, **192**, 511–534.

Lindzen, R. S., 1988: Instability of plane parallel shear flow (toward a mechanistic picture of how it works). *Pageoph*, **126**, 103–121.

Lindzen, R.S., and K.K. Tung, 1978: Wave overreflection and shear instability. *J. Atmos. Sci.*, **35**, 1626–1632.

Lipps, F.B., 1970: Barotropic stability and tropical disturbances. *Mon. Wea. Rev.*, **98**, 122–131.

Magnusdottir, G., and W. H. Schubert, 1990: On the generalization of semi-geostrophic theory to the β-plane. *J. Atmos. Sci.*, **47**, 1714–1720.

Magnusdottir, G., and W. H. Schubert, 1991: Semigeostrophic theory on the hemisphere. *J. Atmos. Sci.*, **48**, 1449–1456.

Mapes, B., and R. A. Houze, Jr., 1992: An integrated view of the 1987 Australian monsoon and mesoscale convective systems. Part I: Horizontal structure. Submitted to *Quart. J. R. Met. Soc.*

Mass, C., 1979: A linear primitive equation model of African wave disturbances. *J. Atmos. Sci.*, **36**, 2075–2092.

McBride, J. L., 1987: The Australian Monsoon. In *Reviews of Monsoon Meteorology*. Edited by C. P. Chang and T. N. Krishnamurti. Oxford University Press, 203–231.

McBride, J. L., B. W. Gunn, G. J. Holland, T. D. Keenan, N. E. Davidson and W. M. Frank, 1989: Time series of total heating and moistening over the Gulf of Carpentaria radiosonde array during AMEX. *Mon. Wea. Rev.*, **117**, 2701–2713.

McBride, J. L., and G. J. Holland, 1989: The Australian Monsoon Experiment (AMEX): early results. *Aust. Met. Mag.*, **37**, 23–35.

McIntyre, M. E., and T. G. Shepherd, 1987: An exact local conservation theorem for finite-amplitude disturbances to non-parallel shear flows, with remarks on Hamiltonian structure and on Arnol'd's stability theorems. *J. Fluid Mech.*, **181**, 527–565.

McIntyre, M. E., and M. A. Weissman, 1978: On radiating instabilities and and resonant overreflection. *J. Atmos. Sci.*, **35**, 1190–1196.

Michalke, A., 1964: On the inviscid instability of the hyperbolic-tangent velocity profile. *J. Fluid Mech.*, **19**, 543–556.

Nitta, T., and M. Yanai, 1969: A note on the barotropic instability of the tropical easterly current. *J. Meteor. Soc. Japan*, **47**, 127–130.

Peng, M. S., and R. T. Williams, 1986: Spatial instability of the barotropic jet with slow streamwise variation. *J. Atmos. Sci.*, **43**, 2430–2442.

Philander, S. G. H., 1976: A note on the stability of the tropical easterlies. *J. Meteor. Soc. Japan*, **54**, 328–330.

Philander, S. G. H., 1978: Instabilities of zonal equatorial currents, II. *J. Geophys. Res.*, **83**, 3679–3682.

Philander, S. G. H., 1990: *El Niño, La Niña, and the Southern Oscillation.* Academic Press, 293 pp.

Pratt, L. J., J. Earles, P. Cornillon and J.-F. Caylula, 1991: The nonlinear behavior of varicose disturbances in a simple model of the Gulf Stream. *Deep-sea Res.*, **38**, S591–S622.

Pratt, L. J., and J. Pedlosky, 1991: Linear and nonlinear barotropic instability of geostrophic shear layers. *J. Fluid Mech.*, **224**, 49–76.

Rayleigh, J. W. S., 1945: *The Theory of Sound, Volume II.* Dover Publications, New York (reprint of the 1894 edition), 504 pages.

Reed, R. J., D. C. Norquist and E. E. Recker, 1977: The structure and properties of African wave disturbances as observed during phase III of GATE. *Mon. Wea. Rev.*, **105**, 317–333.

Rennick, M. A., 1976: The generation of African waves. *J. Atmos. Sci.*, **33**, 1955–1969.

Ripa, P., 1983: General stability conditions for zonal flows in a one-layer model on the beta-plane or the sphere. *J. Fluid Mech.*, **126**, 463–487.

Ripa, P., 1991: General stability conditions for a multi-layer model. *J. Fluid Mech.*, **222**, 119–137.

Schubert, W. H., P. E. Ciesielski, D. E. Stevens and H.-C. Kuo, 1991: Potential vorticity modeling of the ITCZ and the Hadley circulation. *J. Atmos. Sci.*, **48**, 1493–1509.

Shepherd, T. G., 1988a: Rigorous bounds on the nonlinear saturation of instabilities to parallel shear flows. *J. Fluid Mech.*, **196**, 291–322.

Shepherd, T. G., 1988b: Nonlinear saturation of baroclinic instability. Part I: The two-layer model. *J. Atmos. Sci.*, **45**, 2014–2025 .

Shepherd, T. G., 1989: Nonlinear saturation of baroclinic instability. Part II: Continuously stratified fluid. *J. Atmos. Sci.*, **46**, 888–907.

Shepherd, T. G., 1990: Arnol'd stability applied to fluid flow: Successes and failures. *Proceedings of the IMA Workshop on Nonlinear Phenomena in Atmospheric and Oceanic Sciences, June 4–8, 1990*, G. F. Carnevale and R. T. Pierrehumbert, eds., to be published by Springer-Verlag.

Simmons, A. J., 1977: A note on the instability of the African easterly jet. *J. Atmos. Sci.*, **34**, 1670–1674.

Stevens, D. E., 1983: On symmetric stability and instability of zonal mean flows near the equator. *J. Atmos. Sci.*, **40**, 882–893.

Stevens, D. E., and P. E. Ciesielski, 1986: Inertial instability of horizontally sheared flow away from the equator. *J. Atmos. Sci.*, **43**, 2845–2856.

Webster, P. J., and R. A. Houze, Jr., 1991: The Equatorial Mesoscale Experiment (EMEX): An overview. *Bull. Amer. Meteor. Soc.*, **72**, 1481–1505.

Williams, R. T., H. Lim and C.-P. Chang, 1984: Nonlinear and linear effects in an easterly jet with downstream variation. *J. Atmos. Sci.*, **41**, 621–636.

Williams, R. T., T. K. Schminke and R. L. Newman, 1971: Effect of surface friction on the structure of barotropically unstable tropical disturbances. *Mon. Wea. Rev.*, **99**, 778–785.

Yamasaki, M., and M. Wada, 1972: Barotropic instability of an easterly zonal current. *J. Meteor. Soc. Japan*, **50**, 110–121.

Zabusky, N. J., M. H. Hughes and K. V. Roberts, 1979: Contour dynamics for the Euler equations in two dimensions. *J. Comput. Phys.*, **30**, 96–106.

Zabusky, N. J., and E. A. Overman, 1983: Regularization of contour dynamical algorithms. *J. Comput. Phys.*, **52**, 351–373.